

Effects of a spin-flavour dependent interaction on light-flavoured baryon helicity amplitudes

Michael Ronniger^a and Bernard Ch. Metsch

Helmholtz Institute für Strahlen- und Kernphysik (Theorie), Universität Bonn, Nußallee 14-16, D-53115 Bonn, Germany

June 11, 2017

Abstract This paper is a continuation of previous work about the effects of a phenomenological flavour dependent force in a relativistically covariant constituent quark model based on the Salpeter equation on the structure of light-flavoured baryon resonances. Here the longitudinal and transverse helicity amplitudes as studied experimentally in the electro-excitation of nucleon- and Δ resonances are calculated. In particular the amplitudes for the excitation of three and four star resonances as calculated in a previous model \mathcal{A} are compared to those of the novel model \mathcal{C} as well as to existing and partially new experimental data such as *e.g.* determined by the CB-ELSA collaboration. A brief discussion of some improvements to model \mathcal{C} is given after the introduction.

PACS. 11.10.St Bound and unstable states; Bethe-Salpeter equations – 12.39.Ki Relativistic quark model – 13.40.Gp Electromagnetic form factors – 13.40.Hq Electromagnetic decays

1 Introduction

This paper is a continuation of our previous work [1] on the description of baryon resonances in a covariant Bethe-Salpeter framework. While in [1] we concentrated on the description of the mass spectrum in the present paper we discuss the results on electromagnetic transition amplitudes obtained on the basis of the Salpeter amplitudes determined previously. The dynamical ingredients of the relativistically covariant quark model used are instantaneous interaction kernels describing confinement, a spin-flavour dependent interactions kernel motivated by instanton effects as well as in addition a phenomenologically introduced spin-flavour dependent interaction. The latter was found to improve the description obtained previously in [2–4] in particular of Roper-like scalar excitations as well as the position of some negative parity Δ -resonances slightly below 2 GeV. With instantaneous interaction kernels the Bethe-Salpeter equation reduces to the more tractable Salpeter equation which can be cast in the form of an eigenvalue equation for the masses and the Salpeter amplitudes. These in turn determine the vertex functions for any on-shell momentum of the baryons which then enter the electromagnetic current matrix elements. The details of this procedure can be found in [5].

Spin-flavour dependent effective quark-quark interactions have also been studied previously by the Graz group [6–14] which obtained very satisfactory results for the mass spectra up to 1.7 GeV as well as for the corresponding nucleon form factors on the basis of a truncated pseudo-

vector coupled Yukawa potential, where the tensor force terms were neglected. In [1] we found a phenomenological *Ansatz* which includes a short ranged flavour-singlet and a flavour-octet exchange with pseudoscalar-like coupling of Gaussian form to be most effective for the improvements mentioned above. This newly introduced interaction kernel increased the number of parameters of seven in the former model (Model \mathcal{A} , see [3,4]) to ten in the new version (Model \mathcal{C} , see [1]), which we still consider to be acceptable in view of the multitude of baryon masses described accurately in this manner. For the values of the parameters we refer to table 1, where we listed an improved set of parameters for the interaction kernels of model \mathcal{C} together with the values used in [1] displayed in brackets. Likewise the parameters for the interaction kernels of model \mathcal{A} obtained from calculations within a larger model space, see also [1] are listed along with the values (in brackets) as determined in [3,4] in smaller model spaces. Note that the two models \mathcal{A} and \mathcal{C} , specified in table 1 employ different confinement Dirac-structures for the constant part (offset) Γ_0 and the linear part (slope) Γ_s (see [1,3] for more information). All calculations in the present paper are based on the parameter values of table 1.

Furthermore we want to point out, that the calculation of helicity amplitudes or transition form factors (such as that for the nucleon- $\Delta(1232)$ magnetic transition) in lowest order as considered here does not introduce any additional parameter in the underlying models as discussed in [1] before. Since in the new model \mathcal{C} we can account for more baryon excitations accurately we can now also offer predictions for some Δ -resonances which could not be covered before in model \mathcal{A} . In partic-

^a e-mail: ronniger@hiskp.uni-bonn.de

Table 1. Model parameter values for the novel model \mathcal{C} in comparison to those of model \mathcal{A} [3,4]. The bracketed numbers in the column for model \mathcal{A} are the parameters as found in [3, 4] and the numbers above them are recalculated with higher numerical accuracy as commented in [1]. The numbers in the column for model \mathcal{C} represent an improved set with respect to the values quoted in [1] which are listed in brackets. Note that the Dirac structure for the confinement interaction kernel is different in models \mathcal{A} and \mathcal{C} , see also [1].

parameter		model \mathcal{C}	model \mathcal{A}
masses	m_n [MeV]	350.0 [325.0]	330.0
	m_s [MeV]	625.0 [600.0]	670.0
confinement	a [MeV]	-370.8 [-366.8]	-734.6 [-700.0]
	b [MeV/fm]	208.4 [212.86]	453.6 [440.0]
instanton	g_{nn} [MeV fm ³]	317.9 [341.5]	130.3 [136.0]
induced	g_{ns} [MeV fm ³]	260.0 [273.6]	81.8 [96.0]
interaction	λ [fm]	0.4	0.4
octet	$\frac{g_8^2}{4\pi}$ [MeV fm ³]	118.0	–
exchange		[100.86]	
singlet	$\frac{g_0^2}{4\pi}$ [MeV fm ³]	1715.5	–
exchange		[1897.4]	
	$\lambda_8 = \lambda_0$ [fm]	0.25	–

ular these are: $\Delta_{1/2^+}$ (1750), $\Delta_{3/2^+}$ (1600), $\Delta_{1/2^-}$ (1900), $\Delta_{3/2^-}$ (1940) and $\Delta_{5/2^-}$ (1930) as reported in [1]. Additionally there now exists new data for photon decay amplitudes from Anisovich *et al.* [15–17] and for helicity amplitudes from Aznauryan *et al.* [18–21] as well as the MAID analysis [22, 23], in particular the analysis and parametrisations in the recent overview [24], with information also on longitudinal amplitudes which can serve as a test of the present model beyond the comparison done previously in [5, 25, 26] on the basis of the amplitudes determined in model \mathcal{A} of [3]. For the definition of the helicity amplitudes we use the conventions as in Tiator *et al.* [24] as mentioned in Eqs. (7a) to (7c) in the subsequent sec. 3.

The paper is organised as follows: After a brief recapitulation on some improvements concerning model \mathcal{C} in sec. 2 and the determination of the helicity amplitudes for electro-excitation in the Salpeter model, we shall present the results in sec. 3, which contains three subsections: Sec. 3.1.1, covers the helicity amplitudes for the electro-excitation of nucleon resonances, sec. 3.1.2 contains the helicity amplitudes for the electro-excitation of Δ -resonances, while sec. 3.2 summarises the photon decay amplitudes. Sec. 3.3 contains a short discussion of the magnetic and electric transition form factor of the $\Delta(1232)$ resonance before we conclude with a summary in sec. 4.

2 Improvements to model \mathcal{C}

In the course of the investigations within the novel model \mathcal{C} [1] a new parameter set was found which led to an improved description in particular of the nucleon form factors. This new set of parameters is listed in table 1 of the introduction. The corresponding baryon mass spectra are very similar to those published in [1]; only for some higher excitation deviations up to 30 MeV with respect to the values presented in [1] were found. We therefore refrain from displaying the mass spectra here. The calculated masses of those baryons which enter the helicity amplitudes calculated in this work can be found in tables 2 and 3. However for nucleon form factors which were also given in [1] some small but partially significant modifications were found and the results will be discussed subsequently.

In Fig. 1 the calculated electric proton form factor (divided by its dipole-shape)

$$G_D(Q^2) = \frac{1}{(1 + Q^2/M_V^2)^2}, \quad (1)$$

with $M_V^2 = 0.71 \text{ GeV}^2$ (see [27, 28]) in both versions of model \mathcal{C} is compared to experimental data.

It is found that with the new set of parameters model \mathcal{C} describes the data for momenta transfers $Q^2 \lesssim 3 \text{ GeV}^2$ slightly better than with the older set of [1], but the modification is rather small. Fig. 2 shows the electric neu-

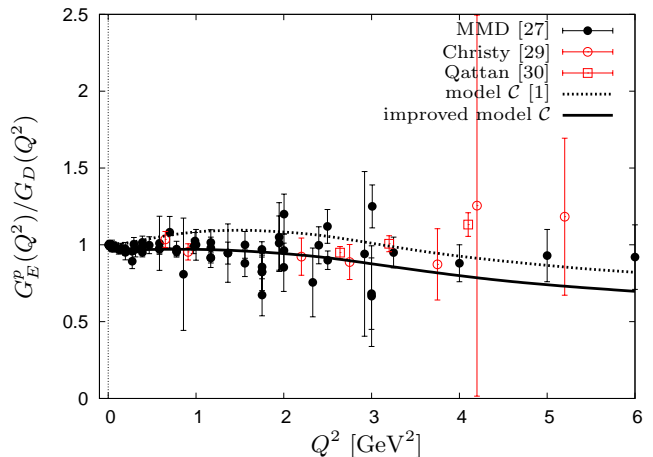


Fig. 1. The electric form factor of the proton divided by the dipole form $G_D(Q^2)$, Eq. (1). MMD-Data are taken from Mergell *et al.* [27], supplemented by data from Christy *et al.* [29] and Qattan *et al.* [30]. The solid line represents the results from model \mathcal{C} with the new set of parameters, while the dashed line those from model \mathcal{C} [1]. Red data points are taken from polarisation experiments and black ones are obtained by Rosenbluth separation.

tron form factor where the effect of the new parameter set yields a significantly improved description, reflecting the fact that this small quantity is thus very sensitive to parameter changes. Although the deviation between both

curves could be interpreted as an estimate of the uncertainty in the model prediction the new version demonstrates that within the model it is indeed possible to account for the momentum transfer dependence and the position of the maximum rather accurately. The new results

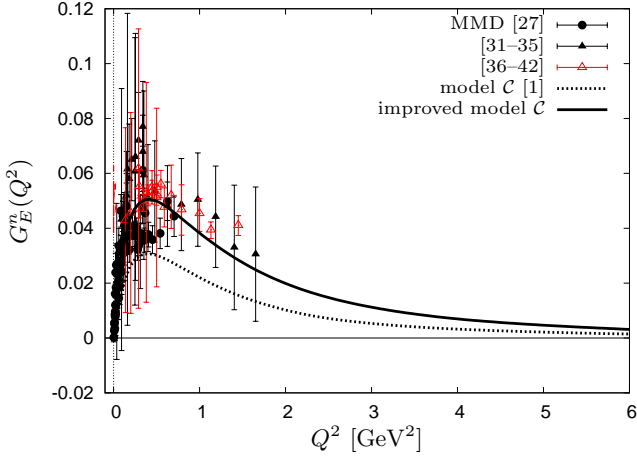


Fig. 2. The electric form factor of the neutron. MMD-Data are taken from the compilation of Mergell *et al.* [27]. The solid line represents the results from the improved model \mathcal{C} ; the dashed line is the result from model \mathcal{C} [1]. Red data points are taken from polarisation experiments and black ones are obtained by Rosenbluth separation.

are very similar to the results from the Bhaduri-Cohler-Nogami quark model quoted as BCN in [12], whereas the older version from [1] is closer to the result quoted as GBE-model in [12].

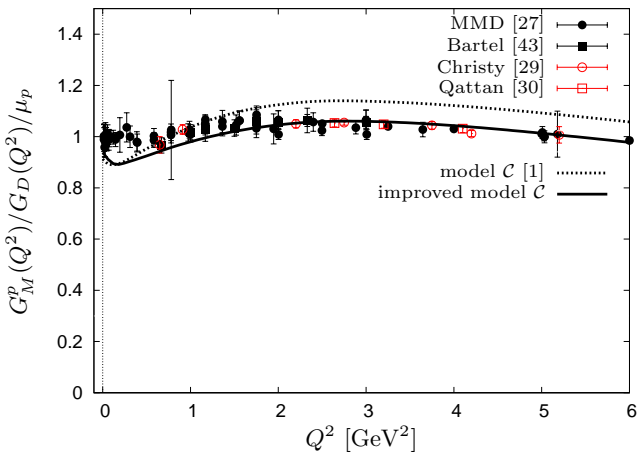


Fig. 3. The magnetic form factor of the proton divided by the dipole form $G_D(Q^2)$, Eq. (1) and the magnetic moment of the proton $\mu_p = 2.793 \mu_N$. MMD-Data are taken from the compilation of Mergell *et al.* [27]. Additionally, polarisation experiments are marked in red. The black marked data points are obtained by Rosenbluth separation.

Also for the magnetic form factors displayed in Fig. 3 and 4 improvements are observed: this concerns in particular the description of the magnetic proton form factor at higher momentum transfers $Q^2 \gtrsim 1 \text{ GeV}^2$.

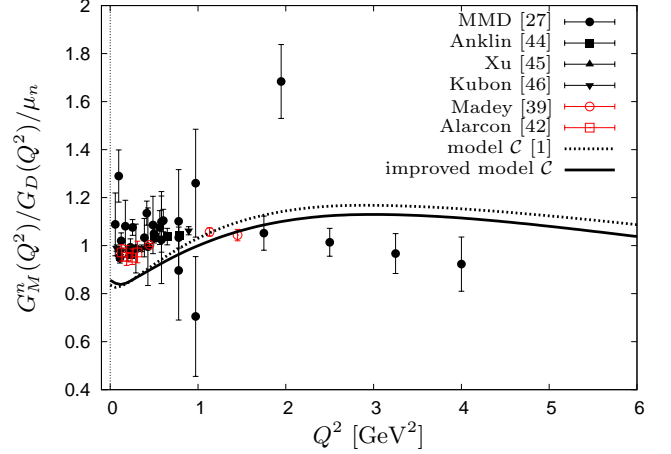


Fig. 4. The magnetic form factor of the neutron divided by the dipole form $G_D(Q^2)$, Eq. (1) and the magnetic moment of the neutron $\mu_n = -1.913 \mu_N$. MMD-Data are taken from the compilation by Mergell *et al.* [27] and from more recent results from MAMI [44,46]. Additionally, polarisation experiments are marked by red data points. The black marked ones are obtained by Rosenbluth separation.

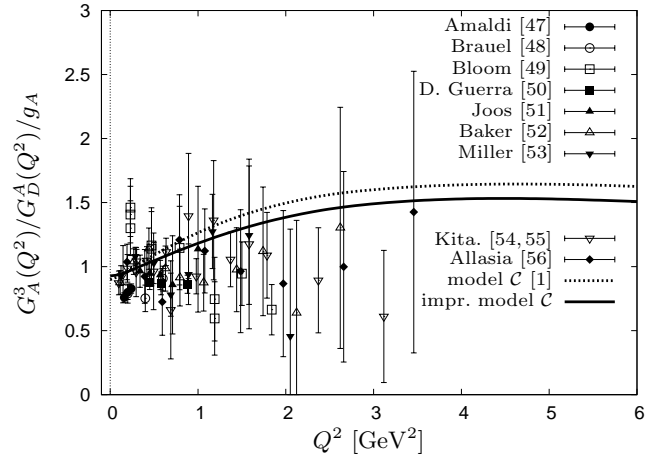


Fig. 5. The axial form factor of the nucleon divided by the axial dipole form in Eq. (2) and the axial coupling $g_A = 1.267$. The solid line is the improved result of model \mathcal{C} , the dashed line the result of model \mathcal{C} in [1]. Experimental data are taken from the compilation by Bernard *et al.* [57].

The axial form factor divided by its dipole-shape

$$G_D^A(Q^2) = \frac{g_A}{(1 + Q^2/M_A^2)^2}, \quad (2)$$

with the parameters $M_A = 1.014 \pm 0.014 \text{ GeV}$ and $g_A = 1.267$ taken from Bodek *et al.* [28] is shown in Fig. 5.

Here a clear preference for either set of parameters cannot be inferred; in general the description is satisfactory in both versions. In subsequent sections all calculations will use the parameters of the improved model \mathcal{C} and shall be quoted simply as model \mathcal{C} .

3 Helicity amplitudes and transition form factors from the current matrix elements

Following the elaboration on the transition current matrix elements in Merten *et al.* [5] one finds in lowest order for a initial baryon state with four-momentum $\bar{P}_i = M_i = (M_i, \mathbf{0})$ in its rest frame and a final baryon state with four-momentum \bar{P}_f the expression

$$\begin{aligned} \langle \bar{P}_f | j^\mu(0) | M_i \rangle &= -3 \int \frac{d^4 p_\xi}{(2\pi)^4} \int \frac{d^4 p_\eta}{(2\pi)^4} \bar{\Gamma}_{\bar{P}_f}^\Lambda(p_\xi, p_\eta - \frac{2}{3}q) \\ & S_F^1(\frac{1}{3}M_i + p_\xi + \frac{1}{2}p_\eta) \otimes S_F^2(\frac{1}{3}M_i - p_\xi + \frac{1}{2}p_\eta) \\ & \otimes S_F^3(\frac{1}{3}M_i - p_\xi - p_\eta + q) \hat{q} \gamma^\mu S_F^3(\frac{1}{3}M_i - p_\xi - p_\eta) \\ & \Gamma_{M_i}^\Lambda(\mathbf{p}_\xi, \mathbf{p}_\eta), \end{aligned} \quad (3)$$

where the so-called vertex-function $\Gamma_{M_i}^\Lambda(\mathbf{p}_\xi, \mathbf{p}_\eta)$ is given in the rest frame by

$$\begin{aligned} \Gamma_{M_i}^\Lambda(\mathbf{p}_\xi, \mathbf{p}_\eta) &:= -i \int \frac{dp'_\xi}{(2\pi)^4} \int \frac{dp'_\eta}{(2\pi)^4} \\ & \left[V_A^{(3)}(\mathbf{p}_\xi, \mathbf{p}_\eta; \mathbf{p}'_\xi, \mathbf{p}'_\eta) + V_A^{\text{eff}}(\mathbf{p}_\xi, \mathbf{p}_\eta; \mathbf{p}'_\xi, \mathbf{p}'_\eta) \right] \\ & \Phi_{M_i}^\Lambda(\mathbf{p}'_\xi, \mathbf{p}'_\eta), \end{aligned} \quad (4)$$

and where the Salpeter-amplitude $\Phi_{M_i}^\Lambda$ is normalised to $\sqrt{2M_i}$. For an arbitrary on-shell momentum \bar{P}_f with $\bar{P}_f^2 = M_f^2$ the vertex function $\Gamma_{\bar{P}_f}^\Lambda(p_\xi, p_\eta - \frac{2}{3}q)$ is obtained from $\Gamma_{M_f}^\Lambda(\mathbf{p}_\xi, \mathbf{p}_\eta)$ by applying a boost. Note that by this procedure we can determine the required vertex function only on the mass shell, which precludes a calculation of transition amplitudes in the time-like region.

The electromagnetic current operator is then defined as

$$j_\mu^E(x) = : \bar{\Psi}(x) \hat{q} \gamma_\mu \Psi(x) : \quad (5)$$

in terms of the charge operator \hat{q} and the quark field-operator $\Psi(x)$. With

$$j_\pm^E(x) = j_1^E(x) \pm i j_2^E(x), \quad (6)$$

and with our normalisation of the Salpeter amplitudes, in accordance with the definitions in Warns *et al.* [58], Tiator *et al.* [24] and Aznauryan and Burkert [21], the transverse and longitudinal helicity amplitudes $A_{1/2}^N$, $A_{3/2}^N$ and $S_{1/2}^N$, respectively, are related to the transition current matrix elements in the rest frame of the baryon B with rest mass

M_B via

$$A_{\frac{1}{2}}^N(Q^2) = \frac{\zeta}{\sqrt{2}} K \left\langle B, M_B, \frac{1}{2} \left| j_+^E(0) \right| N, \bar{P}_N, -\frac{1}{2} \right\rangle, \quad (7a)$$

$$A_{\frac{3}{2}}^N(Q^2) = \frac{\zeta}{\sqrt{2}} K \left\langle B, M_B, \frac{3}{2} \left| j_+^E(0) \right| N, \bar{P}_N, \frac{1}{2} \right\rangle, \quad (7b)$$

$$S_{\frac{1}{2}}^N(Q^2) = \zeta K \left\langle B, M_B, \frac{1}{2} \left| j_0^E(0) \right| N, \bar{P}_N, \frac{1}{2} \right\rangle, \quad (7c)$$

where $K := \sqrt{(\pi \alpha)/(M_N(M_B^2 - M_N^2))}$, α is the fine structure constant, N denotes the ground state nucleon ($N = (p, n)$) with four-momentum $\bar{P}_N = (\sqrt{M_N^2 + \mathbf{k}^2}, -\mathbf{k})$ related to the momentum transfer Q^2 by $\mathbf{k}^2 = (M_B^2 - M_N^2 - Q^2)^2/(4M_B^2) + Q^2$.

Note that the common phase ζ is not determined in the present calculation. In most cases we shall fix ζ such as to reproduce the sign of the proton decay amplitude reported in [59]. Furthermore, note that $\langle p, \bar{P}_N, \frac{1}{2} | j_0^E(0) | p, M_N, \frac{1}{2} \rangle$ is normalised to +1 at $Q^2 = 0$.

3.1 Helicity amplitudes for electro-excitation

In the last decade new experiments were performed at the Jefferson-Laboratory in order to study helicity amplitudes up to 6 GeV². These new experiments were designed to determine the helicity amplitudes for the electro-excitation of the $P_{11}(1440)$, $S_{11}(1535)$ and $D_{13}(1520)$ resonances. The results can be found in [18–20] and [22]. In addition novel data for the longitudinal $S_{1/2}^N$ amplitudes were obtained.

We calculated the corresponding helicity amplitudes of these and other states on the basis of the Salpeter amplitudes obtained in the novel model \mathcal{C} [1]. As mentioned above we are now able to solve the eigenvalue problem with higher numerical accuracy by an expansion into a larger basis which presently includes all three-particle harmonic oscillator states up to an excitation quantum number $N_{\text{max}} = 18$, whereas previously [3–5] the results for baryon masses and amplitudes in model \mathcal{A} were obtained with $N_{\text{max}} = 12$. For comparison and to study the effects of the newly introduced phenomenological flavour-dependent interaction of model \mathcal{C} we thus also recalculated the spectrum and the amplitudes for model \mathcal{A} within the same larger model space. The corresponding changes in the determination of the interaction parameters are indicated in table 1.

3.1.1 Helicity amplitudes for nucleons

We will now turn to the discussion of $N \rightarrow N^*$ helicity amplitudes for each angular momentum J and parity π .

The $J = 1/2$ resonances: A comparison of calculated transverse and longitudinal helicity amplitudes with experimental data for the electro-excitation of the $S_{11}(1535)$ resonance is given in Figs. 6 and 7, respectively. Whereas

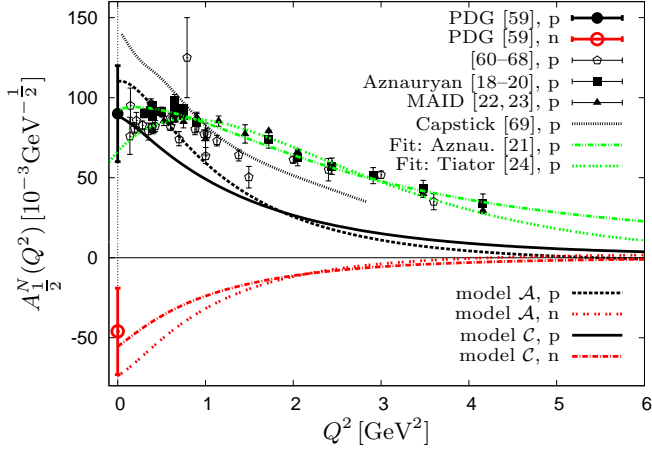


Fig. 6. Comparison of the $S_{11}(1535)$ transverse helicity amplitude $A_{1/2}^N(Q^2)$ for electro-excitation of the proton and the neutron calculated in the model \mathcal{C} (solid and dashed-dotted line) and model \mathcal{A} (dashed lines) to experimental data [18–20, 22, 23, 59–68]. The dotted line is the result obtained by Keister and Capstick [69]. Additionally recent fits obtained by Tiator *et al.* [24] and by Aznauryan *et al.* [21] are displayed as green dotted and dashed-dotted lines, respectively. Note that the results for model \mathcal{A} were recalculated with higher numerical accuracy and thus deviate from the results published previously in [5].

the value of the transverse amplitudes at the photon point ($Q^2 = 0$) both for the proton and the neutron are accurately reproduced in particular by the new model \mathcal{C} , in general the calculated transverse amplitudes are too small by a factor of two; in comparison to the results from model \mathcal{A} the amplitudes of model \mathcal{C} decrease more slowly with increasing momentum transfer, in better agreement with the experimental data. But, in particular the near constancy of the proton data for $0 < Q^2 < 1 \text{ GeV}^2$ is not reflected by any of the calculated results. For comparison we also plotted the results from the quark model calculation of the transverse $A_{1/2}^p$ -amplitude by Keister and Capstick [69] for $Q^2 \lesssim 3 \text{ GeV}^2$ and the fits obtained by Aznauryan *et al.* [21] and Tiator *et al.* [24].

Contrary to this, the momentum transfer dependence of the calculated longitudinal helicity amplitudes hardly bear any resemblance to what has been determined experimentally, in particular the minimum found for the proton at $Q^2 \approx 1.5 \text{ GeV}^2$ is not reproduced. Only the non-relativistic calculation of Capstick and Keister [70] shows a pronounced minimum for the longitudinal $S_{11}(1535)$ amplitude, however this minimum is predicted at the wrong position.

Also the calculated transverse proton helicity amplitude $A_{1/2}^p$ for the next $S_{11}(1650)$ resonance shows a large disagreement with experimental data as shown in Fig. 8. This discrepancy was already found in the previous calculation of Merten *et al.* [5] and obviously is not resolved within model \mathcal{C} . Note, however that the neutron amplitude $A_{1/2}^n$ calculated at the photon point does correspond

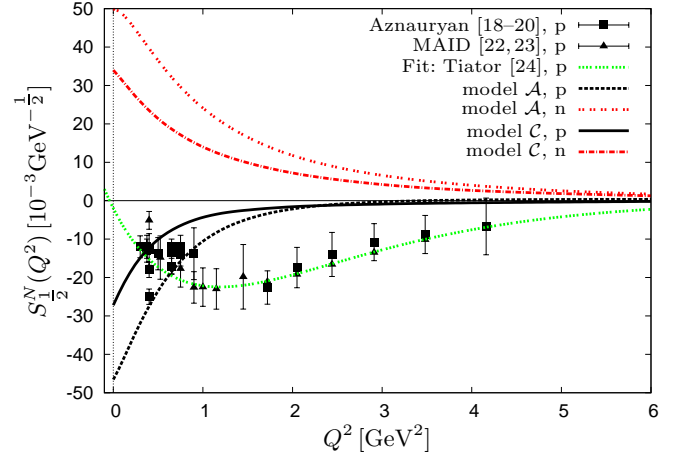


Fig. 7. Comparison of the $S_{11}(1535)$ longitudinal electro-excitation helicity amplitude $S_{1/2}^N(Q^2)$ of proton and neutron calculated in model \mathcal{C} (solid and dashed-dotted line) and model \mathcal{A} (dashed lines) with experimental data [18–20, 22, 23]. Note that for the data points of the MAID-analysis by Tiator *et al.* [23] no errors are quoted. See also caption to Fig. 6.

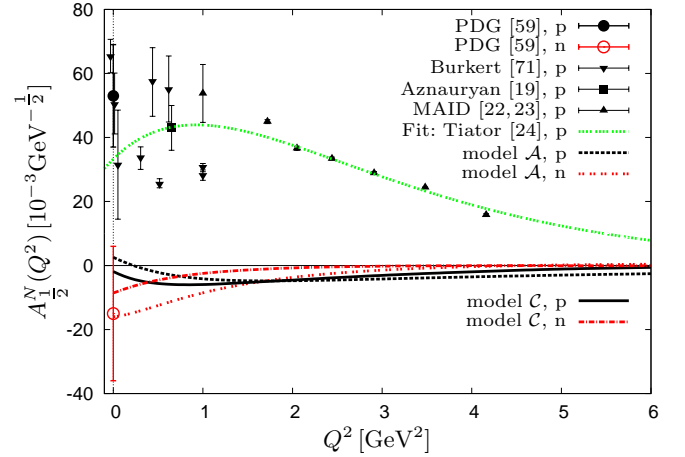


Fig. 8. Comparison of the $S_{11}(1650)$ transverse electro-excitation helicity amplitude $A_{1/2}^N(Q^2)$ of proton and neutron calculated in model \mathcal{C} (solid and dashed-dotted line) and model \mathcal{A} (dashed lines) to experimental data from [19, 22, 23, 59, 71]. See also caption to Fig. 6.

to the data from PDG [59], as illustrated in Fig. 8. The rather small longitudinal $S_{11}(1650)$ amplitude $S_{1/2}^N$ seems to agree with the scarce medium Q^2 data from the MAID-analysis of [22, 23], however for lower Q^2 the single data point of Aznauryan *et al.* [19] seems to indicate a zero crossing of this amplitude not reproduced by either of the model calculations of the $S_{1/2}^p$ -amplitude for the $S_{11}(1650)$ -resonance (see Fig. 9).

The third and fourth $J^\pi = 1/2^-$ nucleon resonances are predicted in model \mathcal{A} at 1872 MeV and 1886 MeV and in model \mathcal{C} at 1839 MeV and 1882 MeV, respectively. Indeed within the Bonn-Gatchina Analysis of the CB-ELSA collaboration data [17] evidence for a $J^\pi = 1/2^-$ nucleon resonance at 1895 MeV was found. As can be seen from

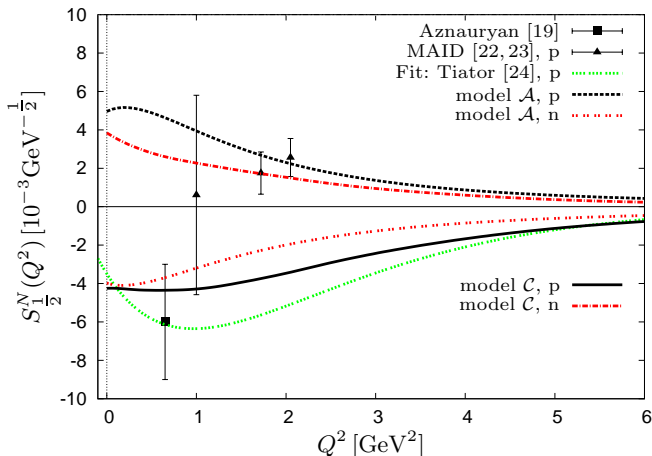


Fig. 9. Comparison of the $S_{11}(1650)$ longitudinal electro-excitation helicity amplitude $S_{1/2}^N$ of proton and neutron calculated in model \mathcal{C} (solid and dashed-dotted line) and model \mathcal{A} (dashed lines). See also caption to Fig. 6.

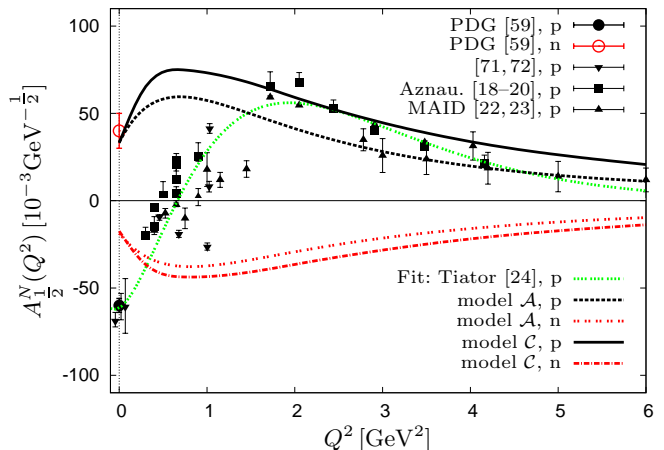


Fig. 11. Comparison of the $P_{11}(1440)$ transverse helicity amplitude $A_{1/2}^N$ for proton and neutron calculated in model \mathcal{C} (solid and dashed-dotted line) and model \mathcal{A} (dashed lines). See also caption to Fig. 6.

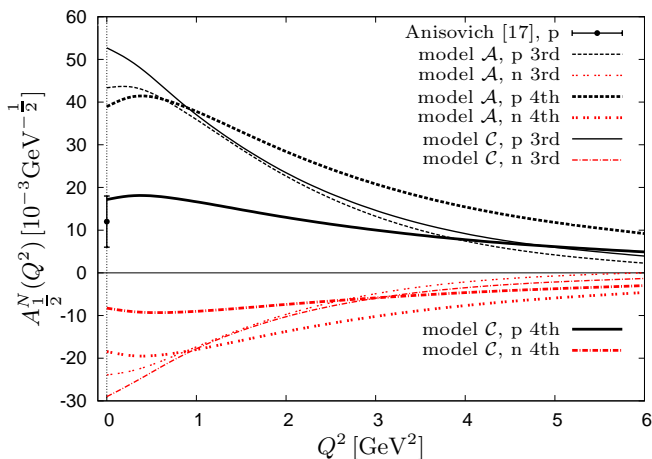


Fig. 10. Comparison of the $S_{11}(1895)$ transverse helicity amplitude $A_{1/2}^N$ for proton and neutron calculated in model \mathcal{C} (solid and dashed-dotted line) and model \mathcal{A} (dashed lines) with the single photon point value from Anisovich *et al.* [15]. See also caption to Fig. 6.

Fig. 10 the predicted transverse amplitudes for the third resonance both models are rather large and the calculated value at the photon point ($Q^2 = 0$) is much larger than the experimental value quoted in [15, 17], but the value of the fourth resonance matches the PDG photon decay amplitude.

The transverse and longitudinal helicity amplitudes of the Roper resonance $P_{11}(1440)$ are displayed in Figs. 11 and 12, respectively. It is obvious, that the zero crossing found in the data at $Q^2 \approx 0.5 \text{ GeV}^2$, see Fig. 11, is not reproduced in the calculated curves, although the Q^2 dependence of the positive values at higher momentum transfers can be accounted for in both models after changing the sign of the old prediction [5]. On the other hand we do find a satisfactory description of the longitudinal

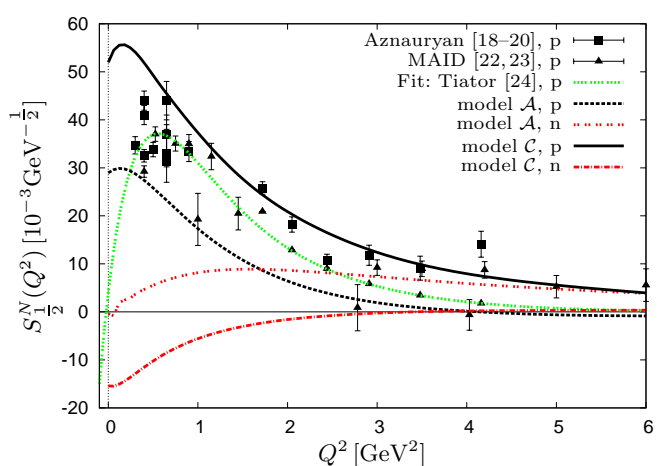


Fig. 12. Comparison of the $P_{11}(1440)$ longitudinal helicity amplitude $S_{1/2}^N$ for proton and neutron calculated in model \mathcal{C} (solid and dashed-dotted line) and model \mathcal{A} (dashed lines). Note that for the data points of the MAID-analysis by Tiator *et al.* [23] no errors are quoted. See also caption to Fig. 6.

$C_{1/2}^p$ -amplitude displayed in Fig. 12 in particular in the new model \mathcal{C} .

Helicity amplitudes of higher lying resonances in the P_{11} channel are only poorly studied in experiments. Nevertheless we shall discuss briefly the $P_{11}(1710)$ helicity amplitude before treating the higher excitations $P_{11}(1880)$ and $P_{11}(2100)$. For the $P_{11}(1710)$ resonance only the photon decay amplitude is reported [59]. In Figs. 13 and 14 we display our predictions for these amplitudes. The transverse $A_{1/2}^N$ -amplitude of model \mathcal{C} matches the PDG data at the photon point in contrast to model \mathcal{A} , which overestimates the proton- and neutron amplitudes by a factor of two. On the other hand this would be in accordance with the larger value obtained by Anisovich *et al.* [17],

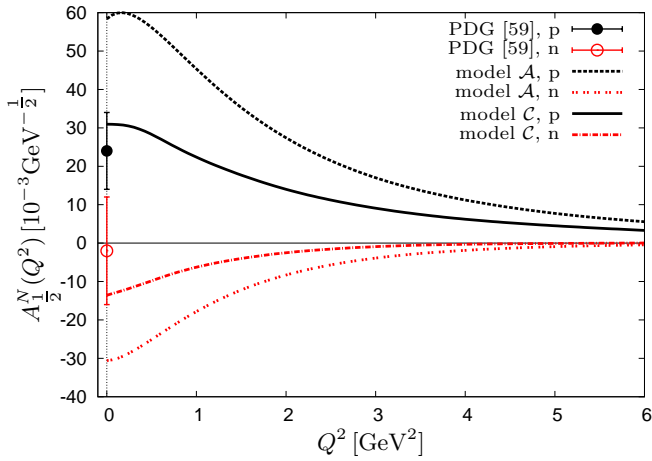


Fig. 13. Comparison of the $P_{11}(1710)$ transverse helicity amplitude $A_{1/2}^N(Q^2)$ for proton and neutron calculated in model C (solid and dashed-dotted line) and model A (dashed lines). See also caption to Fig. 6.

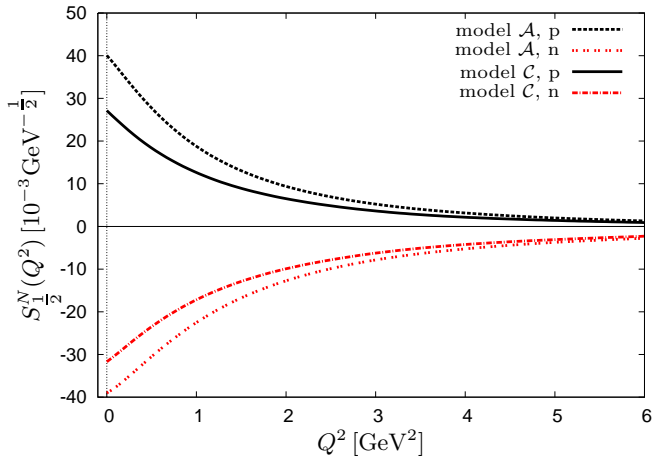


Fig. 14. Prediction of the $P_{11}(1710)$ longitudinal helicity amplitude $S_{1/2}^N(Q^2)$ for proton and neutron calculated in model C (solid and dashed-dotted line) and model A (dashed lines). See also caption to Fig. 6.

$A_{1/2}^p = (52 \pm 15) \times 10^{-3} \text{ GeV}^2$. The prediction of the longitudinal $S_{1/2}^N$ -amplitudes is given in Fig. 14.

Finally we present the results for the fourth and fifth $J^\pi = \frac{1}{2}^+$ -nucleon state in Fig. 15, where we show the transverse helicity amplitudes only. The corresponding masses predicted by model A are 1905 MeV for the fourth and 1953 MeV for the fifth state; for model C the predicted masses are 1872 MeV and 1968 MeV, respectively. The two data at the photon point marked "01" and "02" were obtained by the CB-ELSA collaboration within the Bonn-Gatchina Analysis as reported in [15, 17] for the $N_{1/2}^+(1880)$ resonance. They correspond to two different partial wave solutions in order to extract the corresponding baryon mass and helicity amplitudes. The prediction for the fourth state lies between these values, the values

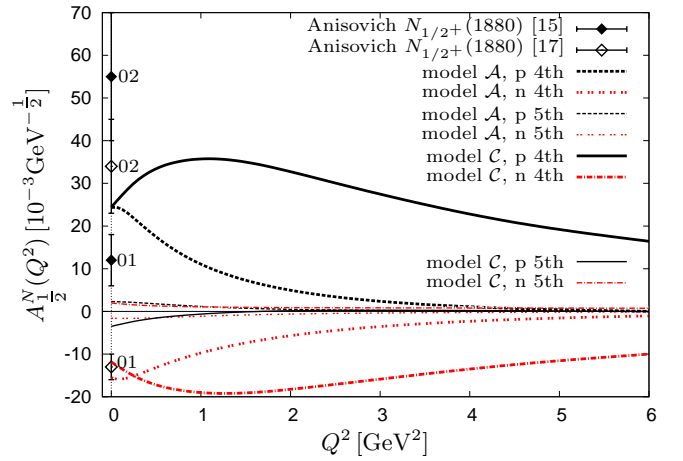


Fig. 15. Prediction of the P_{11} transverse helicity amplitudes $A_{1/2}^N(Q^2)$ for the third and fourth excitation of the proton and the neutron calculated within model C (solid and dashed-dotted lines) and model A (dashed lines). The data at the photon point marked "01" and "02" were reported in [15, 17] as alternatives for the $N_{1/2}^+(1880)$ resonance. See also caption to Fig. 6.

found for the fifth state are much smaller. This also applies for higher $J^\pi = \frac{1}{2}^+$ excitations not displayed here.

The $J = 3/2$ resonances: In Figs. 16 and 17 the transverse helicity amplitudes of the $P_{13}(1720)$ resonance are displayed. Although a reasonable agreement with the data

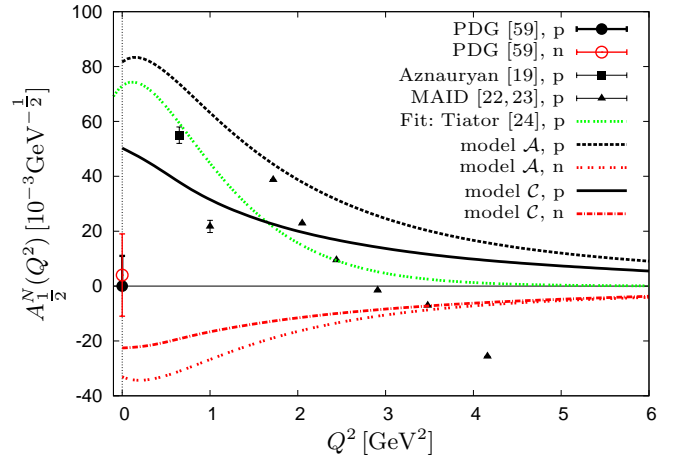


Fig. 16. Comparison of the $P_{13}(1720)$ transverse helicity amplitude $A_{1/2}^N(Q^2)$ of proton and neutron calculated in model C (solid and dashed-dotted line) and model A (dashed lines). Note that for the data points of the MAID-analysis by Tiator *et al.* [23] no errors are quoted. See also caption to Fig. 6.

of Aznauryan *et al.* [19] and with the photon decay amplitude is found for both models, the data from the MAID analysis [22, 23] indicate a sign change for the $A_{1/2}^p$ amplitude at $Q^2 \approx 3 \text{ GeV}^2$ not reproduced by either model. In

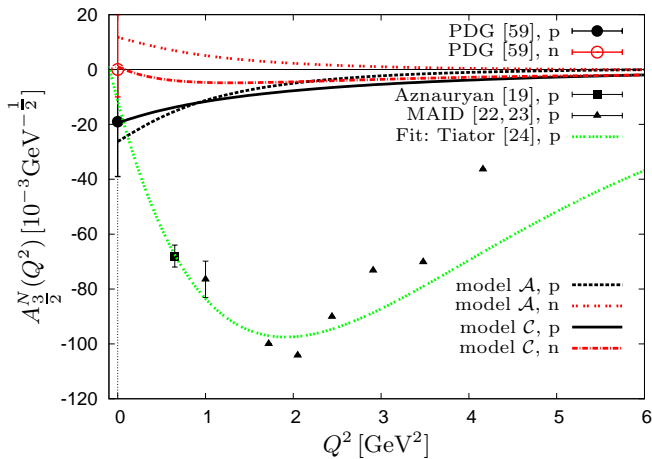


Fig. 17. Comparison of the $P_{13}(1720)$ transverse helicity amplitude $A_{3/2}^N(Q^2)$ of proton and neutron calculated in model \mathcal{C} (solid and dashed-dotted line) and model \mathcal{A} (dashed lines). Note that for the data points of the MAID-analysis by Tiator *et al.* [23] no errors are quoted. See also caption to Fig. 6.

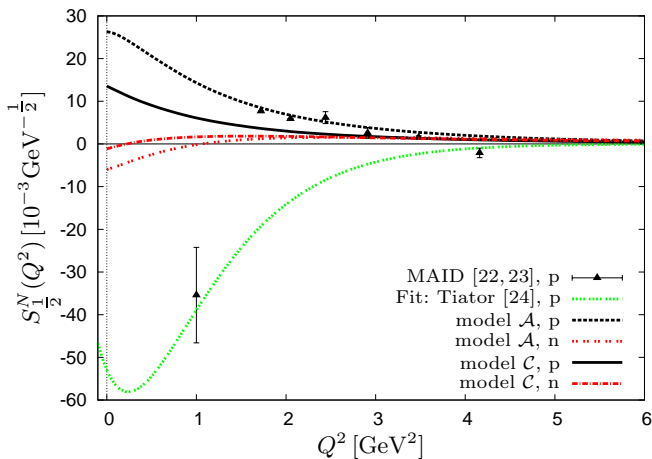


Fig. 18. Comparison of the $P_{13}(1720)$ longitudinal electro-excitation helicity amplitude $S_{1/2}^N(Q^2)$ of proton and neutron calculated in model \mathcal{C} (solid and dashed-dotted line) and model \mathcal{A} (dashed lines). Note that for the data points of the MAID-analysis by Tiator *et al.* [23] no errors are quoted. See also caption to Fig. 6.

spite of not being able to account at all for the large $A_{3/2}^p$ amplitude found experimentally, the longitudinal helicity amplitude as reported in the MAID analysis with exception of the value at $Q^2 \approx 1 \text{ GeV}^2$ is reproduced by both models rather well, as shown in Fig. 18.

For the transverse helicity amplitude $A_{1/2}^p$ (see Fig. 19) of the $D_{13}(1520)$ -resonance we find a reasonable quantitative agreement with experimental data for low momentum transfers, while apart from the fact that in model \mathcal{C} the amplitude is too small by about a factor of two the Q^2 dependence is reproduced up to $Q^2 \approx 6 \text{ GeV}^2$. The minimum at $Q^2 \approx 1 \text{ GeV}^2$ is clearly visible for model \mathcal{A} whereas this feature is not so pronounced in model \mathcal{C} . The $A_{3/2}^p$ -amplitudes are displayed in Fig. 20; here both

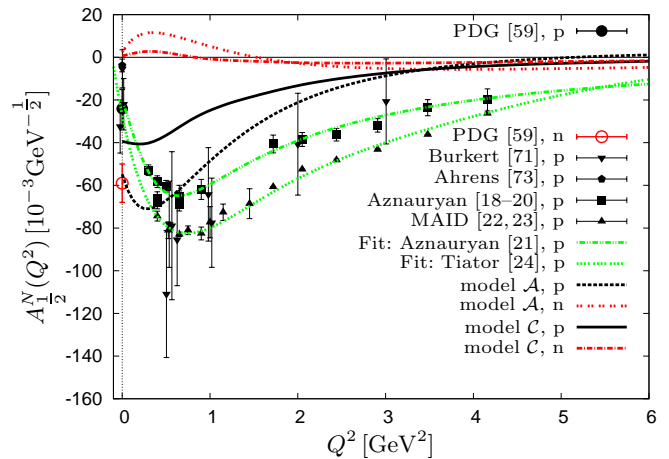


Fig. 19. Comparison of the $D_{13}(1520)$ transverse helicity amplitude $A_{1/2}^N(Q^2)$ of proton and neutron calculated in model \mathcal{C} (solid and dashed-dotted line) and model \mathcal{A} (dashed lines). See also caption to Fig. 6.

model underestimates the data by more than a factor of three. Likewise the calculated neutron $A_{1/2}^n$ - and $A_{3/2}^n$ -

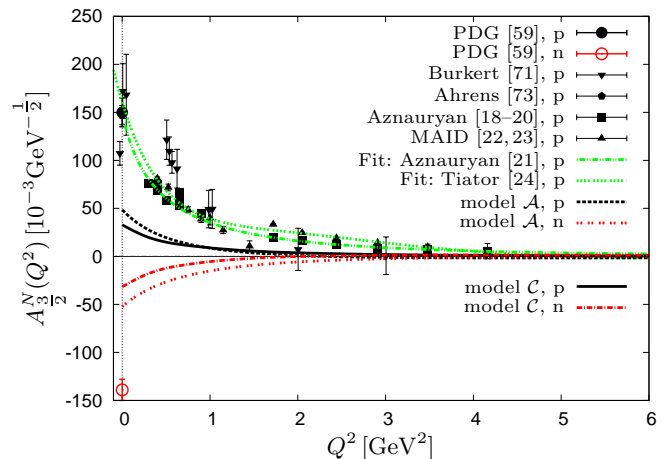


Fig. 20. Comparison of the $D_{13}(1520)$ transverse helicity amplitude $A_{3/2}^N(Q^2)$ for proton and neutron calculated in model \mathcal{C} (solid and dashed-dotted line) and model \mathcal{A} (dashed lines). See also caption to Fig. 6.

amplitudes at the photon point are too small. In particular for the $A_{1/2}^n$ -amplitude the predicted value close to zero is in contradiction to the experimental value $-59 \pm 9 \times 10^{-3} \text{ GeV}^{-1/2}$ from PDG [59]. Unfortunately, although the Q^2 dependence of the magnitude of the longitudinal amplitude $S_{1/2}^p$, see Fig. 21, would describe the experimental data of Aznauryan *et al.* [18–20] and MAID [22] very well, the amplitude has the wrong sign. Note that although, as mentioned above, the common phase ζ in the definition of the helicity amplitudes is not determined in our framework, relative signs between the three helicity amplitudes are fixed.

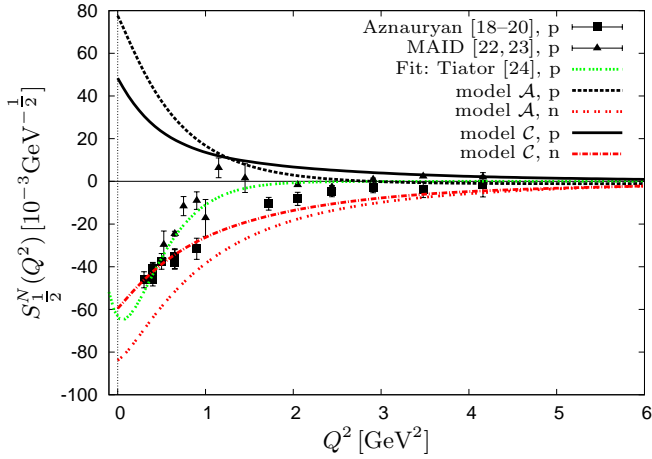


Fig. 21. Comparison of the $D_{13}(1520)$ longitudinal helicity amplitude $S_{1/2}^N(Q^2)$ for proton and neutron calculated in model C (solid and dashed-dotted line) and model A (dashed lines). See also caption to Fig. 6.

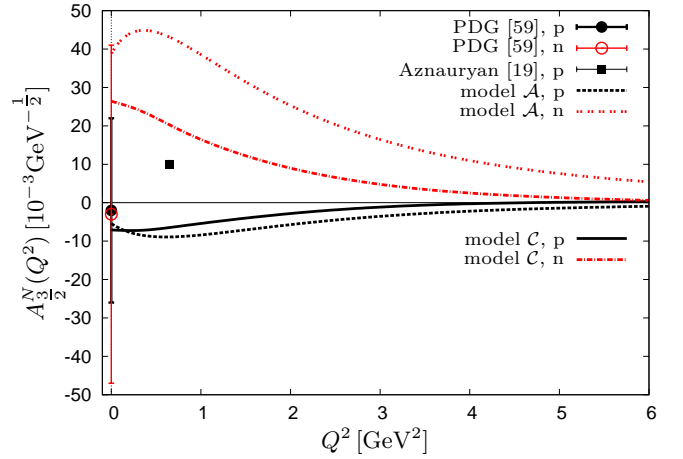


Fig. 23. Comparison of the $D_{13}(1700)$ transverse helicity amplitude $A_{3/2}^N(Q^2)$ for proton and neutron calculated in model C (solid and dashed-dotted line) and model A (dashed lines). See also caption to Fig. 6.

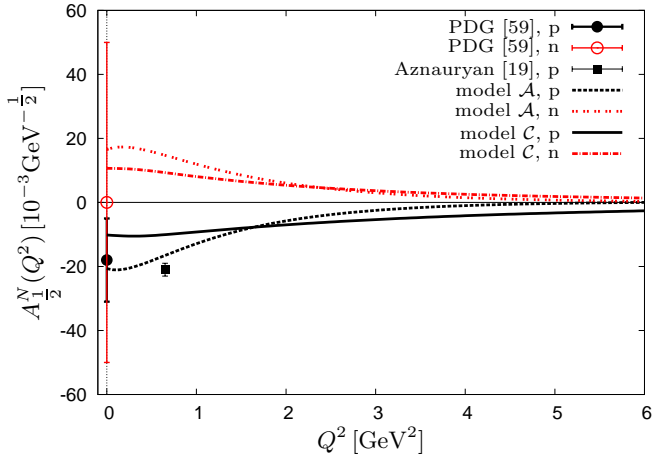


Fig. 22. Comparison of the $D_{13}(1700)$ transverse helicity amplitude $A_{1/2}^N(Q^2)$ for proton and neutron calculated in model C (solid and dashed-dotted line) and model A (dashed lines). See also caption to Fig. 6.

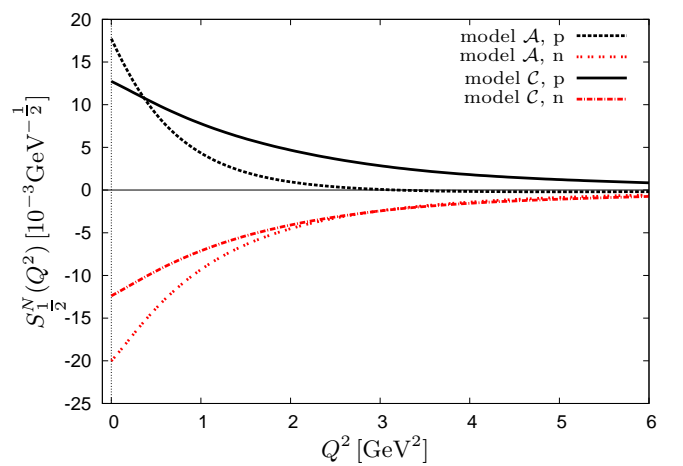


Fig. 24. Prediction of the $D_{13}(1700)$ longitudinal helicity amplitude $S_{1/2}^N(Q^2)$ for proton and neutron calculated in model C (solid and dashed-dotted line) and model A (dashed lines). See also caption to Fig. 6.

The transverse amplitudes for the next $3/2^-$ nucleon resonance, *i.e.* $D_{13}(1700)$, are displayed in Figs. 22 and 23. In contrast to the situation for the $D_{13}(1520)$ -resonance described above, here both models are in accordance with the PDG-data [59] as well as with the data from Aznauryan *et al.* [19] for the $A_{1/2}$ -amplitude, whereas the $A_{3/2}$ -amplitude only reproduces the PDG-data [59] and not the data point from Aznauryan *et al.* [19] at finite momentum transfer. The prediction for the longitudinal $D_{13}(1700)$ amplitudes is given in Fig. 24. The calculated amplitudes turn out to be rather small.

The $J = 5/2$ resonances: Although the transverse $D_{15}(1675)$ helicity amplitudes at the photon point reproduce the experimental data from MAID [22, 23] and the PDG [59] rather well, as displayed in Figs. 25 and 26, both

calculations cannot account for the apparent zero of the experimental $A_{1/2}^P$ -amplitude at $Q^2 \approx 1.5 \text{ GeV}^2$. Furthermore the $A_{3/2}^P$ -amplitude, displayed in Fig. 26 is severely underestimated in magnitude by both models and model C even yields the wrong sign. The transverse amplitudes for the neutron are predicted to be negative, here the calculated value at the photon point for model A is closer to the experimental value than for model C . The longitudinal amplitudes are calculated to be very small for both models. There exists only experimental data from the MAID-analysis [23], indicating that the experimental values are consistent with zero (see Fig. 30).

There also exist data for the helicity amplitudes of the $F_{15}(1680)$ -resonance. The comparison with the calculated values is given in Figs. 28 and 29. In particular in model C a reasonable description of the $A_{1/2}^P$ amplitudes is

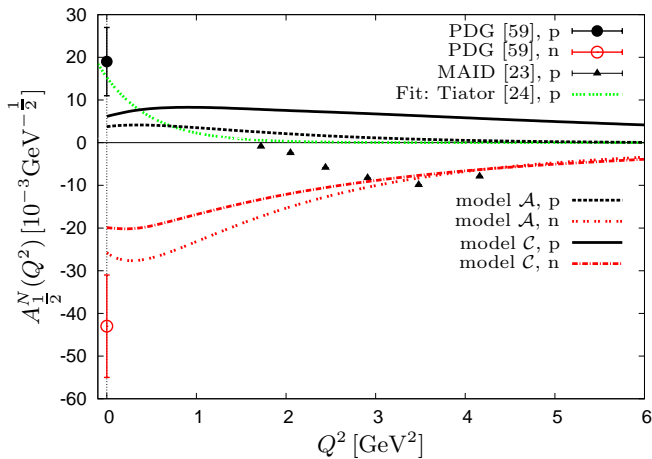


Fig. 25. Comparison of the $D_{15}(1675)$ transverse helicity amplitude $A_{1/2}^N$ for proton and neutron calculated in model \mathcal{C} (solid and dashed-dotted line) and model \mathcal{A} (dashed lines). See also caption to Fig. 6.

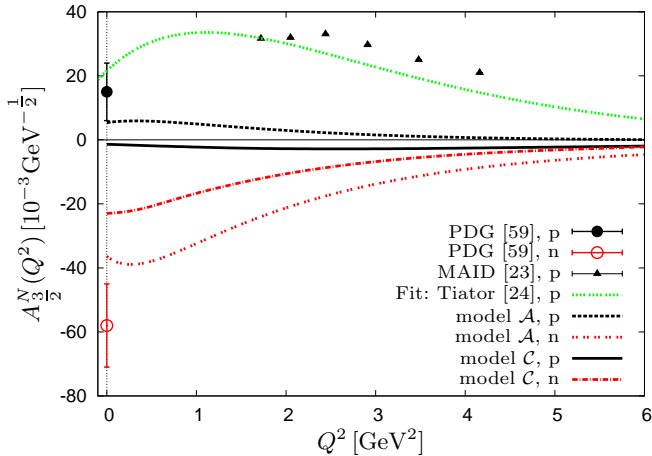


Fig. 26. Comparison of the $D_{15}(1675)$ transverse electro-excitation helicity amplitude $A_{3/2}^N$ for proton and neutron calculated in model \mathcal{C} (solid and dashed-dotted line) and model \mathcal{A} (dashed lines). See also caption to Fig. 6.

found for the newer data from Aznauryan *et al.* [18,19] and MAID [22,23] both at the photon point and for the values at higher momentum transfers. The calculated values in model \mathcal{A} are in better accordance with the the older data from Burkert *et al.* [71] which are larger in magnitude. In contrast to this the $A_{3/2}^p$ -amplitudes are again severely underestimated in magnitude, see Fig. 29. In contrast, for the longitudinal $S_{1/2}^p$ -amplitude we observe a rather good agreement with the data as displayed in Fig. 30, the values obtained in model \mathcal{C} being too small at lower momentum transfers.

The $J = 7/2$ resonances: For positive parity PDG [59] lists the $F_{17}(1990)$ resonance rated with two stars. Both in model \mathcal{A} and in model \mathcal{C} we can relate this to states with a calculated mass of 1954 MeV and 1997 MeV, re-

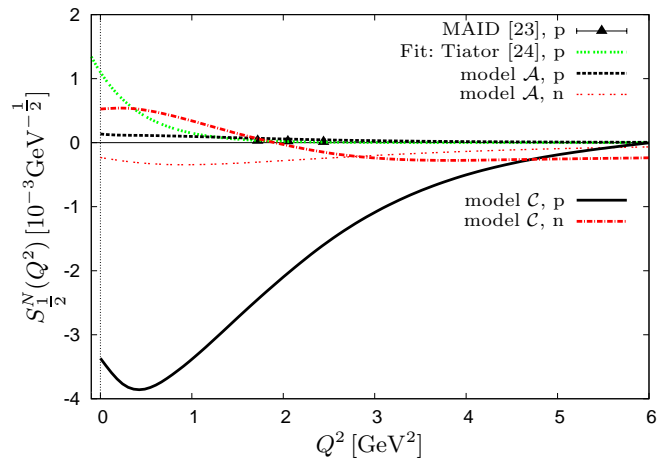


Fig. 27. Comparison of the $D_{15}(1675)$ longitudinal helicity amplitude $S_{1/2}^N$ for proton and neutron calculated in model \mathcal{C} (solid and dashed-dotted line) and model \mathcal{A} (dashed lines). See also caption to Fig. 6.

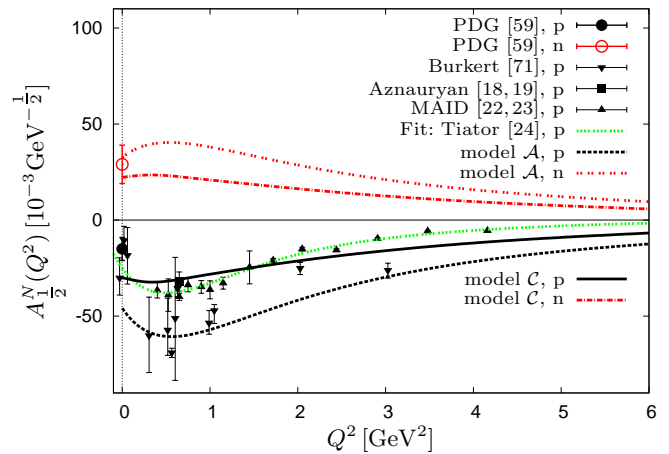


Fig. 28. Comparison of the $F_{15}(1680)$ transverse helicity amplitude $A_{1/2}^N$ for proton and neutron calculated in model \mathcal{C} (solid and dashed-dotted line) and model \mathcal{A} (dashed lines). See also caption to Fig. 6.

spectively. The corresponding photon amplitudes are very small, see Table 2. Otherwise, concerning the $J = 7/2$ resonances there exists only one negative parity resonance with more than at least a three star rating, the $G_{17}(2190)$. The corresponding predictions for transverse and longitudinal helicity amplitudes are shown in Figs. 31 and 32.

The $J = 9/2$ resonances: The transverse and longitudinal helicity amplitudes of the $J^\pi = 9/2^+$ resonance $G_{19}(2250)$ are predicted to be very small as shown in Figs. 33 and 34 and coincide with the estimate by Anisovich *et al.* [17] for the transverse amplitudes. Obviously, the $A_{3/2}^p$ amplitude of model \mathcal{C} and the longitudinal amplitudes of model \mathcal{A} are effectively zero.

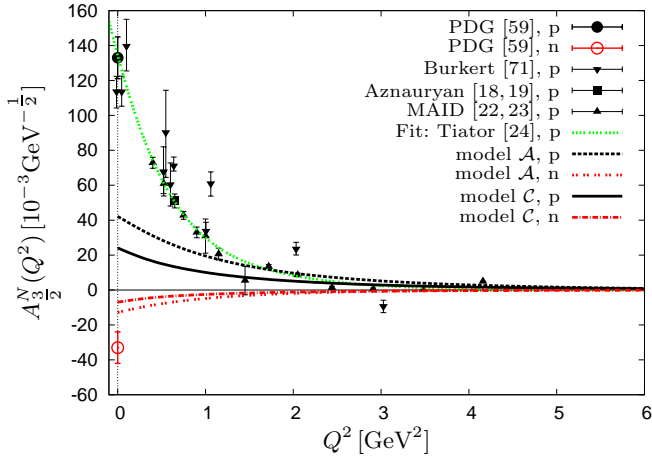


Fig. 29. Comparison of the $F_{15}(1680)$ transverse helicity amplitude $A_{3/2}^N(Q^2)$ for proton and neutron calculated in model \mathcal{C} (solid and dashed-dotted line) and model \mathcal{A} (dashed line). See also caption to Fig. 6.

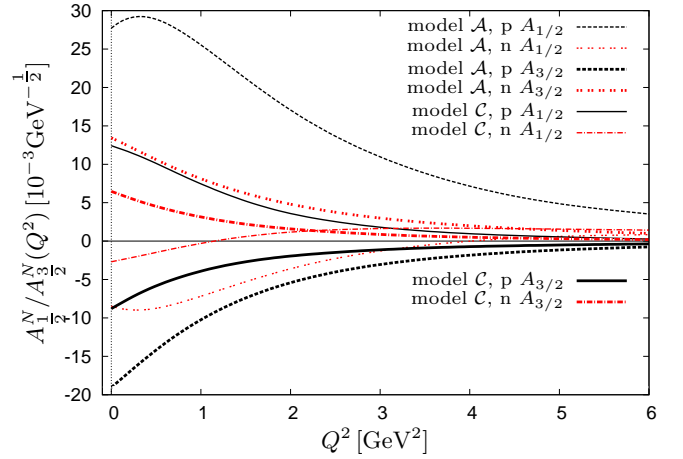


Fig. 31. Prediction of the $G_{17}(2190)$ transverse helicity amplitudes $A_{1/2}^N$ and $A_{3/2}^N$ for proton and neutron calculated in model \mathcal{C} (solid and dashed-dotted line) and model \mathcal{A} (dashed lines). See also caption to Fig. 6.

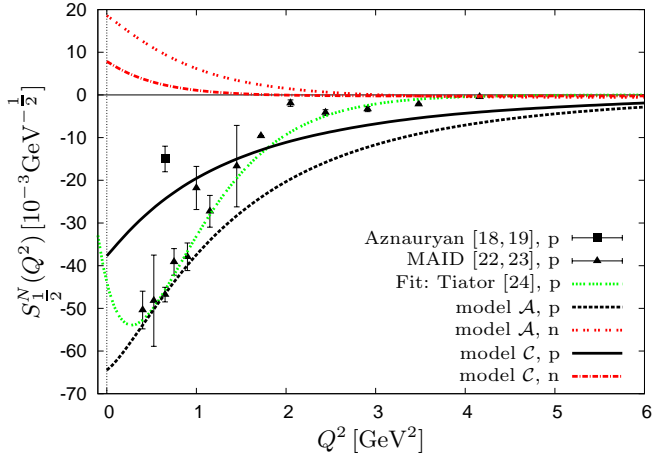


Fig. 30. Comparison of the $F_{15}(1680)$ longitudinal helicity amplitude $S_{1/2}^N(Q^2)$ for proton and neutron calculated in model \mathcal{C} (solid and dashed-dotted line) and model \mathcal{A} (dashed lines). See also caption to Fig. 6.

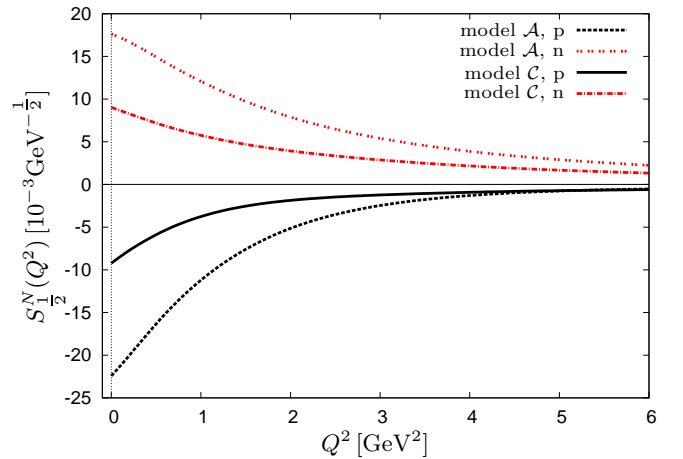


Fig. 32. Prediction of the $G_{17}(2190)$ longitudinal helicity amplitude $S_{1/2}^N(Q^2)$ for proton and neutron calculated in model \mathcal{C} (solid and dashed-dotted line) and model \mathcal{A} (dashed lines). See also caption to Fig. 6.

Although the resonance with $J^\pi = 9/2^-$, $H_{19}(2220)$ has a four star rating by the PDG, only the proton photon decay amplitude has been estimated in [17]. The calculated values are displayed in Fig. 35 and Fig. 36; the amplitudes turn out to be smaller in model \mathcal{C} than in model \mathcal{A} in better agreement with the estimate of [17].

The $J = 11/2$ resonances: Figs. 37 and 38 shows predictions of the transverse and longitudinal helicity amplitudes for the $J^\pi = 1/2^-$ $I_{111}(2600)$ -resonances. So far no data available.

3.1.2 Nucleon $\rightarrow \Delta$ helicity amplitudes

We now turn to a discussion of the results for $N \rightarrow \Delta$ electro-excitation.

The $J = 1/2$ resonances: We start the discussion with the negative parity $S_{31}(1620)$ -resonance. For the $S_{31}(1620)$ transverse and longitudinal helicity amplitudes, depicted in Fig. 39, a wide variety of experimental data at and near the photon point exists. The calculated values lie well within the region of experimental data obtained due to the spread in partially contradictory experimental data but an assessment of the quality is hardly possible. The positive longitudinal amplitude $S_{1/2}^N$ in Fig. 39 as determined in [22, 23] together with the single data point from [19] suggest a sign change in the region $Q^2 \approx 0.7 - 1.0 \text{ GeV}^2$ not reproduced by both calculations, this clearly needs more experimental clarification.

The next excitation in this channel is the $S_{31}(1900)$ resonance; the corresponding transverse and longitudinal helicity amplitudes are displayed in Fig. 40. Here we only give the results for model \mathcal{C} since the original model \mathcal{A}

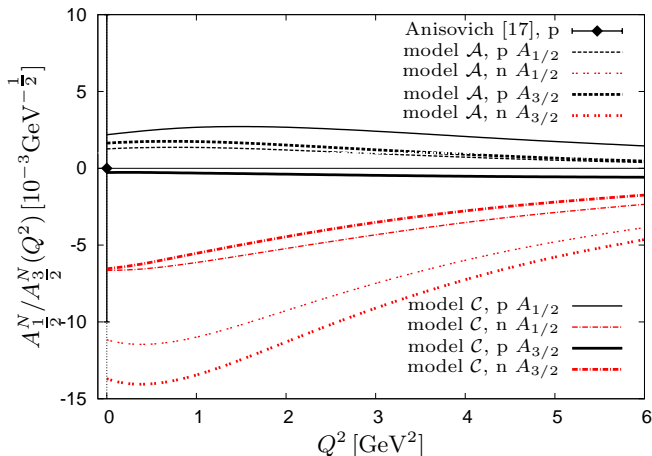


Fig. 33. Comparison of the $G_{19}(2250)$ transverse helicity amplitudes $A_{1/2}^N$ and $A_{3/2}^N$ for proton and neutron calculated in model C (solid and dashed-dotted line) and model A (dashed lines). The error bar at the photon point corresponds to an estimate by Anisovich *et al.* [17] for $A_{1/2}^N$ and $A_{3/2}^N$ within $|A^p| < 10 \times 10^{-3} \text{ GeV}^{-1/2}$. See also caption to Fig. 6.

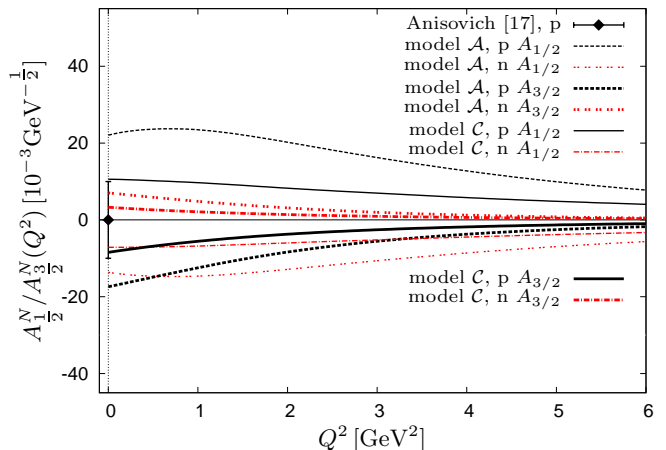


Fig. 35. Comparison of the $H_{19}(2220)$ transverse helicity amplitudes $A_{1/2}^N$ and $A_{3/2}^N$ for proton and neutron calculated in model C (solid and dashed-dotted lines) and model A (dashed lines). The error bar at the photon point corresponds to an estimate by Anisovich *et al.* [17] for $A_{1/2}^N$ and $A_{3/2}^N$ within $|A^p| < 10 \times 10^{-3} \text{ GeV}^{-1/2}$. See also caption to Fig. 6.

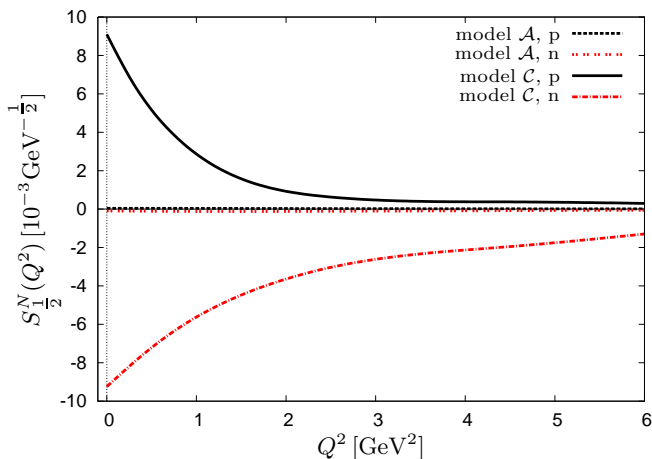


Fig. 34. Prediction of the $G_{19}(2250)$ longitudinal helicity amplitude $S_{1/2}^N$ for proton and neutron calculated in model C (solid and dashed-dotted line) and model A (dashed lines). See also caption to Fig. 6.

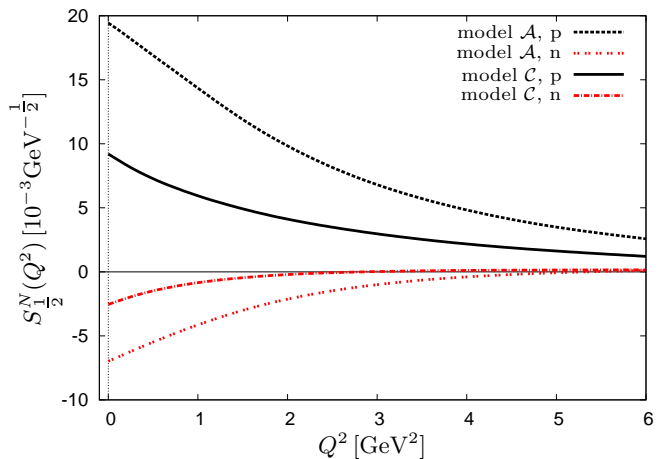


Fig. 36. Prediction of the $H_{19}(2220)$ longitudinal helicity amplitude $S_{1/2}^N$ for proton and neutron calculated in model C (solid and dashed-dotted line) and model A (dashed lines). See also caption to Fig. 6.

does not describe a resonance in this region. The values at the photon point seems to be in better agreement with the data from Crawford *et al.* [75] than with the data from Awaaji *et al.* [74] and Anisovich *et al.* [17]. Note that for both S_{31} -resonances we judiciously fixed the phase ζ in order to reproduce the sign of the PDG value at the photon point, as has been mentioned above. Reversing the sign of ζ would in case of the $S_{31}(1620)$ -resonance in fact better reproduce the data at larger momentum transfers.

Also the lowest positive parity Δ -resonance $P_{31}(1750)$ is only reproduced in model C as shown in [1]. The calculation does not account for the large value found by Penner *et al.* [76] at the photon point, see Fig. 41. The longitudinal amplitude is predicted to be negative for this resonance.

The helicity amplitudes for the next excited state, $P_{31}(1910)$ are shown in Fig. 42. Note that model A does produce two nearby resonances at the position of the $P_{31}(1910)$ resonance, see [1,3]. The calculated amplitudes for both resonances as well as the calculated amplitude in model C are very small and in rough agreement with the experimental value found at the photon point which has a large error. Again the assessment cannot be conclusive. Also shown are the predictions for the rather small longitudinal amplitudes.

The $J = 3/2$ resonances: We shall discuss the electro-excitation of the ground-state Δ resonance, $P_{33}(1232)$ in some more detail below; the transverse amplitudes are

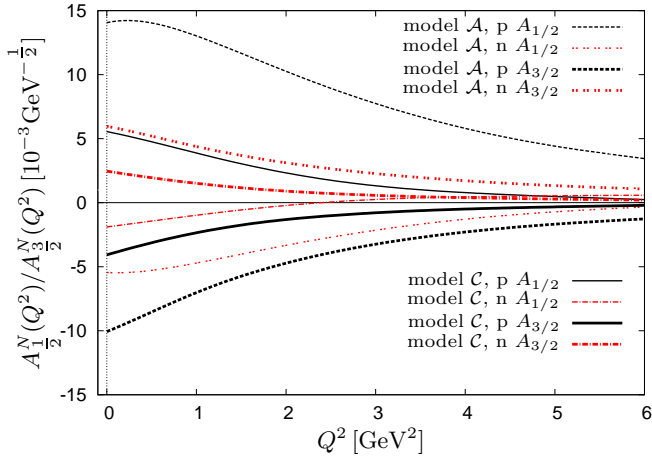


Fig. 37. Prediction of the $I_{111}(2600)$ transverse helicity amplitudes $A_{1/2}^N$ and $A_{3/2}^N$ for proton and neutron calculated in model C (solid and dashed-dotted line) and model A (dashed lines). See also caption to Fig. 6.

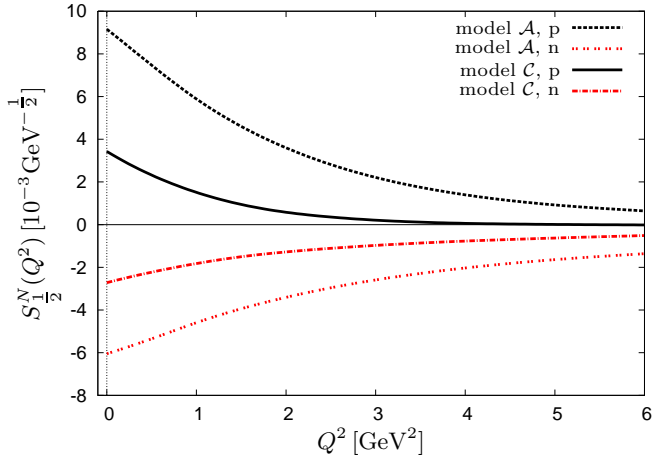


Fig. 38. Prediction of the $I_{111}(2600)$ longitudinal helicity amplitude $S_{1/2}^N$ for proton and neutron calculated in model C (solid and dashed-dotted line) and model A (dashed lines). See also caption to Fig. 6.

shown in Fig. 43 while Fig. 44 displays the results for the longitudinal amplitude. With the exception of the low momentum transfer region $Q^2 < 0.5 \text{ GeV}^2$ we observe a fair agreement with experimental data for the transverse amplitude $A_{1/2}^N$ for both models, which, however, both show a minimum in the amplitudes for $Q^2 \lesssim 0.5 \text{ GeV}^2$ (which, in contradiction to data, also persists in the magnetic form factor, see Fig. 56), whereas the data show a minimum of some kinematical origin at much smaller momentum transfers $Q^2 \lesssim 0.1 \text{ GeV}^2$. Also the experimental data for the $S_{1/2}^N$ helicity amplitude can be accounted for by the calculated curve for model C at the highest momentum transfers only, while the amplitude calculated in A is much smaller. Note that more data is available for the magnetic transition form factor, which is a linear combination of the $A_{1/2}^N$ and $A_{3/2}^N$ amplitudes, see sec. 3.3.

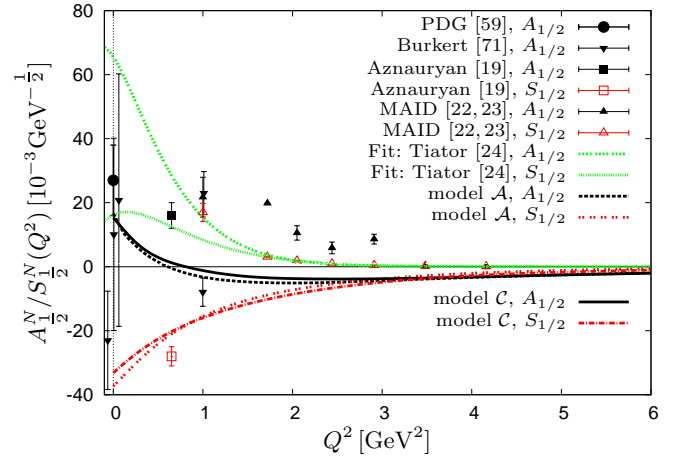


Fig. 39. Comparison of the $S_{31}(1620)$ transverse and the longitudinal helicity amplitudes $A_{1/2}^N$ and $S_{1/2}^N$ calculated in model C (solid and dashed-dotted line) and model A (dashed lines) with experimental data from [19,22,23,59,71]. Note that for the data points of the MAID-analysis by Tiator *et al.* [23] no errors are quoted. See also caption to Fig. 6.

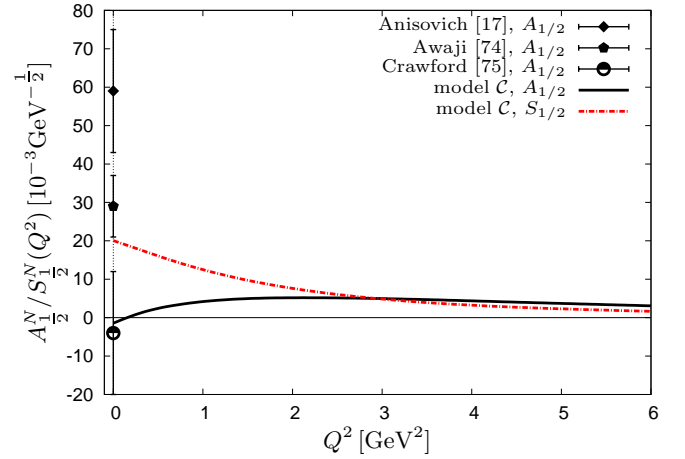


Fig. 40. Comparison of the $S_{31}(1900)$ transverse $A_{1/2}^N$ (solid and dashed-dotted line) and longitudinal helicity amplitude $S_{1/2}^N$ (dashed-dotted line) in model C. See also caption to Fig. 6.

The Roper-like excitation of the ground state Δ resonance, $P_{33}(1600)$, is only described adequately in model C. The corresponding helicity amplitudes $A_{1/2}^N$, $A_{3/2}^N$ and $S_{1/2}^N$ are displayed in Fig. 45. The $A_{1/2}^N$ amplitude is calculated to be smaller than the decay amplitude quoted by the PDG [59]. Contrary to this we find a rather large $A_{3/2}^N$ amplitude with a pronounced minimum around $Q^2 \approx 0.75 \text{ GeV}^2$. However in this case the value at the photon point is overestimated.

For the $P_{33}(1920)$ state with positive parity the helicity amplitudes are displayed in Figs. 46 and 47. In [1] it is shown that there exist several states around 1920 MeV which correspond to the second and third excited $\Delta_{3/2}^+$ state and which are predicted at 1834 MeV and at 1912

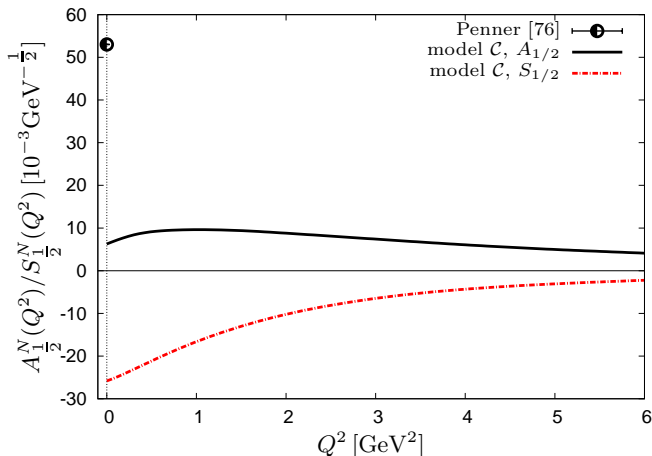


Fig. 41. Comparison of the $P_{31}(1750)$ transverse $A_{1/2}^N$ and longitudinal $S_{1/2}^N$ helicity amplitude calculated in model \mathcal{C} (solid line) and the data from Penner *et al.* [76]. See also caption to Fig. 6.

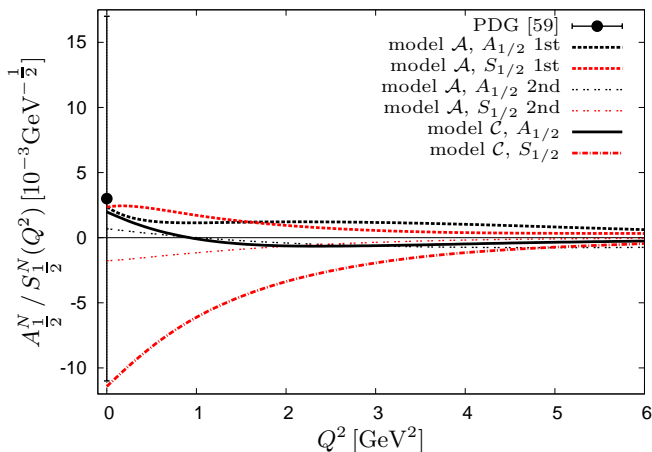


Fig. 42. Comparison of the $P_{31}(1910)$ transverse $A_{1/2}^N$ and longitudinal $S_{1/2}^N$ helicity amplitude calculated in model \mathcal{C} (solid and dashed-dotted line) and model \mathcal{A} (dashed lines). See also caption to Fig. 6.

MeV for model \mathcal{A} and at 1899 MeV and at 1932 MeV for model \mathcal{C} , respectively. The transverse amplitudes are in general very small and match the photon decay data of [74, 76, 77] whereas the data of Anisovich *et al.* [17] cannot be reproduced. The predictions for the longitudinal amplitude as well as the $A_{3/2}^N$ amplitude for the third excitation are effectively zero.

We now turn to negative parity excited Δ -resonances. For the $D_{33}(1700)$ transition amplitudes we find that the predictions of both models are rather close, as displayed in Figs. 48 and 49. Note that the calculated masses of the $D_{33}(1700)$ -resonance, *viz.* $M = 1594$ MeV for model \mathcal{A} and $M = 1600$ MeV for model \mathcal{C} , are about 100 MeV lower than the experimental mass at approximately 1700 MeV. This of course affects the pre-factors in Eqs. (7a) and (7b) leading to the conclusion that the current matrix elements

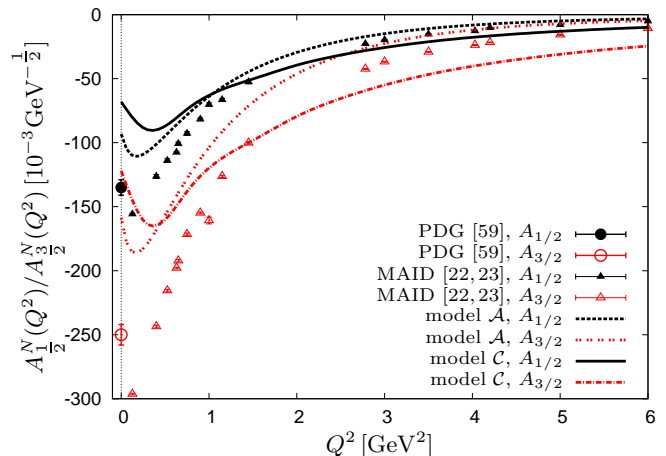


Fig. 43. Comparison of the $P_{33}(1232)$ transverse helicity amplitudes $A_{1/2}^N$ and $A_{3/2}^N$ as calculated in model \mathcal{C} (solid and dashed-dotted line) and model \mathcal{A} (dashed lines). See also caption to Fig. 6 and the magnetic and electric transition form factor in Figs. 56 and 57, respectively.

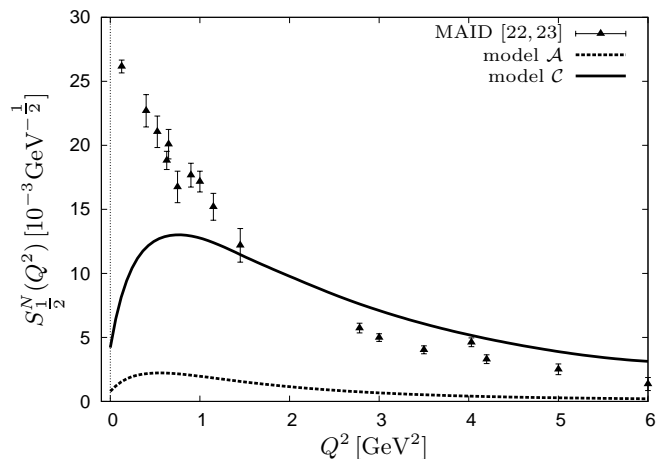


Fig. 44. Comparison of the $P_{33}(1232)$ longitudinal helicity amplitude $S_{1/2}^N$ calculated in model \mathcal{C} (solid line) and model \mathcal{A} (dashed line) to experimental data from [22, 23, 59]. See also caption to Fig. 6 and the Coulomb transition form factor in Fig. 58.

are calculated to be too small. For the transverse amplitude $A_{1/2}^N$ only the single data point from Aznauryan *et al.* [19] is close to the calculated curves. At the photon point the calculated values also agree with the PDG data [59]. In contrast the data from MAID [22, 23] and Burkert *et al.* [71] cannot be accounted for. Similar observations are made for the $A_{3/2}^N$ -amplitude. The longitudinal $S_{1/2}^N$ amplitude has a sign opposite to the rare data from Aznauryan *et al.* [19] and MAID [22, 23] as shown in Fig. 49. Note however that the MAID-analysis of Tiator *et al.* [23] yields a vanishing $S_{1/2}^N$ amplitude in contrast to the appreciable amplitudes found in the calculations.

Figs. 50 and 51 contain the prediction for the transverse and longitudinal helicity amplitudes of the $D_{33}(1940)$

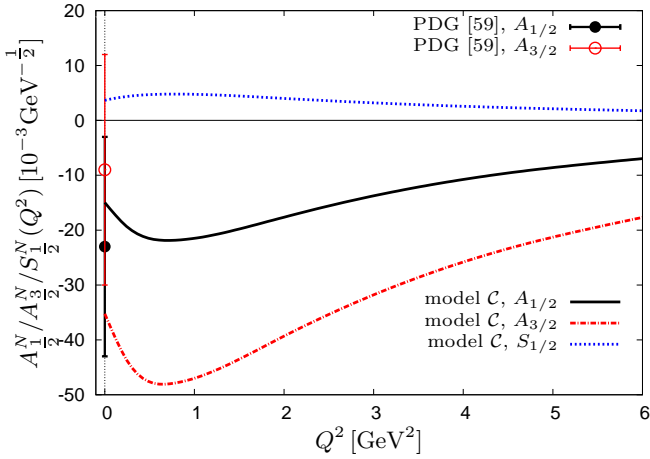


Fig. 45. Comparison of the $P_{33}(1600)$ transverse and longitudinal helicity amplitudes $A_{1/2}^N$, $A_{3/2}^N$ and $S_{1/2}^N$ calculated in model \mathcal{C} with the PDG-data [59] and [17]. See also caption to Fig. 6.

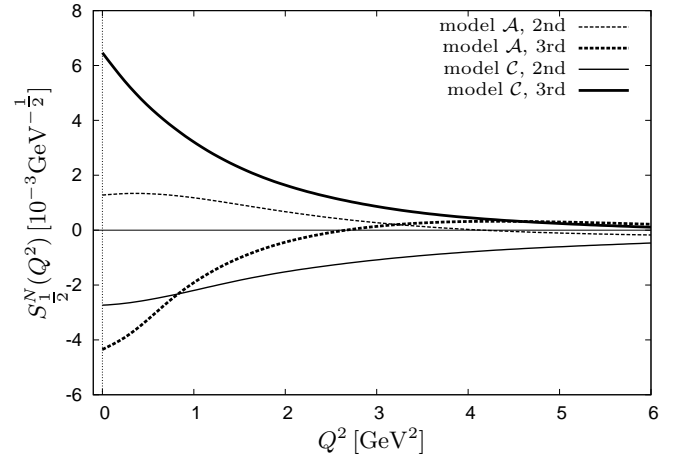


Fig. 47. Prediction of the $P_{33}(1920)$ longitudinal helicity amplitude $S_{1/2}^N$ calculated in model \mathcal{C} (solid lines) and model \mathcal{A} (dashed lines). See also caption to Fig. 6.

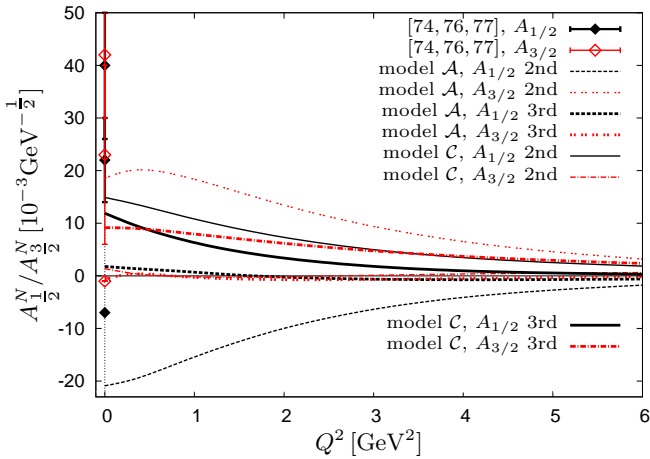


Fig. 46. Comparison of the $P_{33}(1920)$ transverse helicity amplitudes $A_{1/2}^N$ and $A_{3/2}^N$ as calculated in model \mathcal{C} (solid and dashed-dotted line) and model \mathcal{A} (dashed lines) with the data from [74, 76, 77]. Note that the values at $Q^2 = 0$ of Anisovich *et al.* [17], $A_{1/2}^p = 130_{-60}^{+30} \times 10^{-3} \text{GeV}^{-1/2}$ and $A_{3/2}^p = -150_{-50}^{+25} \times 10^{-3} \text{GeV}^{-1/2}$, are beyond the range displayed. See also caption to Fig. 6.

resonance in model \mathcal{C} . Note that in this model two resonances with masses $M = 1895 \text{ MeV}$ and $M = 1959 \text{ MeV}$ are predicted in this energy range, as shown in [1]. Accordingly we have displayed two alternative predictions for the helicity amplitudes. The results for the transverse amplitudes, see Fig. 50, for both resonances are rather similar; the measured photon decay amplitudes from Horn *et al.* [77] and Awaji *et al.* [74] are in conflict, the calculated values favour a small negative value at the photon point, which agrees with the data from Awaji *et al.* [74]. In Fig. 51 we also show the corresponding longitudinal amplitudes.

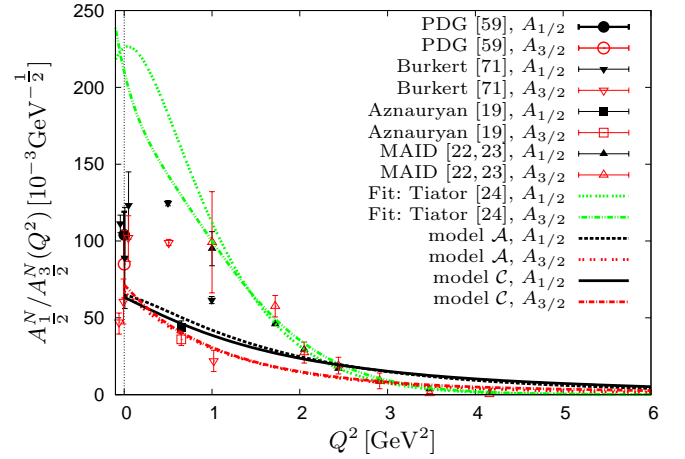


Fig. 48. Comparison of the $D_{33}(1700)$ transverse helicity amplitudes $A_{1/2}^N$ and $A_{3/2}^N$ calculated in model \mathcal{C} (solid and dashed-dotted line) and model \mathcal{A} (dashed lines). See also caption to Fig. 6.

The $J = 5/2$ resonances: In Fig. 52 we show the $A_{1/2}^N$, $A_{3/2}^N$ and $S_{1/2}^N$ helicity amplitudes calculated in model \mathcal{C} [1] for the $D_{35}(1930)$ resonance. Also displayed is the PDG-data at the photon point [59], where we find that the transverse amplitudes agree well with the experimental values. The longitudinal amplitude is found to be almost vanishing. Since model \mathcal{A} cannot account for a resonance in this energy region no results are given in this case.

Both models are able to reproduce the lowest $J = 5/2$ Δ resonance with positive parity. The prediction of the helicity amplitudes of the $F_{35}(1905)$ can be found in Fig. 53. Both models can account very well for the PDG-data at the photon point for the $A_{1/2}$ transverse amplitudes, but the $A_{3/2}$ amplitude is found with a sign opposite to that of the data. As for the previously discussed resonance the results for the longitudinal amplitudes turn out to be very small.

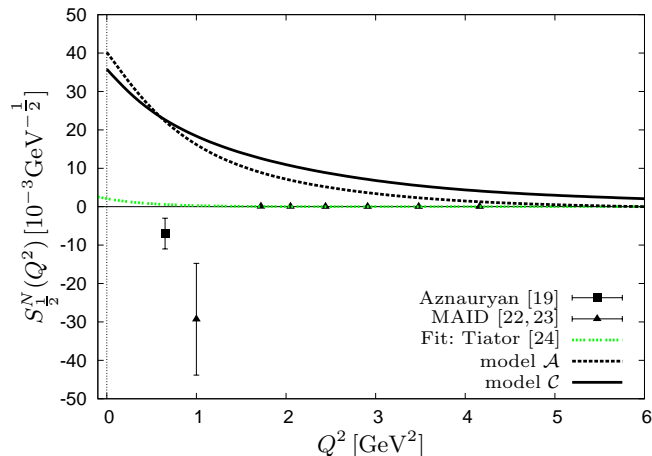


Fig. 49. Comparison of the $D_{33}(1700)$ longitudinal helicity amplitude $S_{1/2}^N$ of the nucleon calculated in model \mathcal{C} (solid line) and model \mathcal{A} (dashed line). Note that for the data points of the MAID-analysis by Tiator *et al.* [23] no errors are quoted. See also caption to Fig. 6.

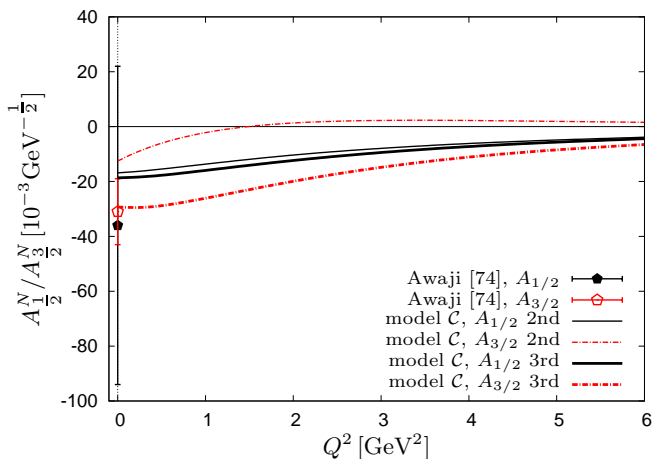


Fig. 50. Comparison of the $D_{33}(1940)$ transverse helicity amplitudes $A_{1/2}^N$ (solid lines) and $A_{3/2}^N$ (dashed lines) calculated in model \mathcal{C} with the data from Awaji *et al.* [74]. Due to the fact that model \mathcal{C} offers two alternatives for the $D_{33}(1940)$ -resonance, as shown in [1], both amplitudes, labelled with "second" and "third" are displayed. Note that the values at $Q^2 = 0$ of Horn *et al.* [77], $A_{1/2}^p = (160 \pm 40) \times 10^{-3} \text{GeV}^{-1/2}$ and $A_{3/2}^p = (130 \pm 30) \times 10^{-3} \text{GeV}^{-1/2}$, are beyond the range displayed. See also caption to Fig. 6.

The $J = 7/2$ resonances: For $J = 7/2$ there exists only one four star resonance, the $F_{37}(1950)$. The predictions of the corresponding transverse and longitudinal helicity amplitudes are shown in Fig. 54. Here the predictions of the transverse amplitudes are much too small in order to explain the experimental photon couplings.

The $J = 11/2$ resonances: Fig. 55 shows the prediction of the transverse and longitudinal helicity amplitudes of the $\Delta_{11/2^+}(2420)$ resonance. The amplitudes found in

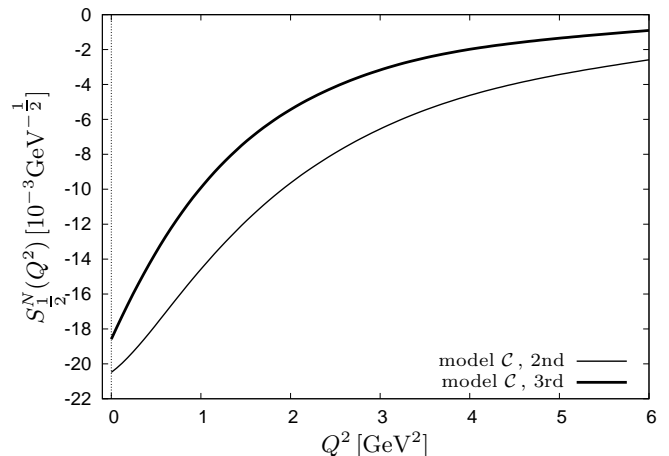


Fig. 51. Prediction of the $D_{33}(1940)$ longitudinal electro-excitation helicity amplitudes $S_{1/2}^N$ of the nucleon calculated in model \mathcal{C} . Due to the fact that model \mathcal{C} offers two alternatives for the $D_{33}(1940)$ -resonance, as shown in [1], both amplitudes, labelled with "first" and "second" are displayed. See also caption to Fig. 6.

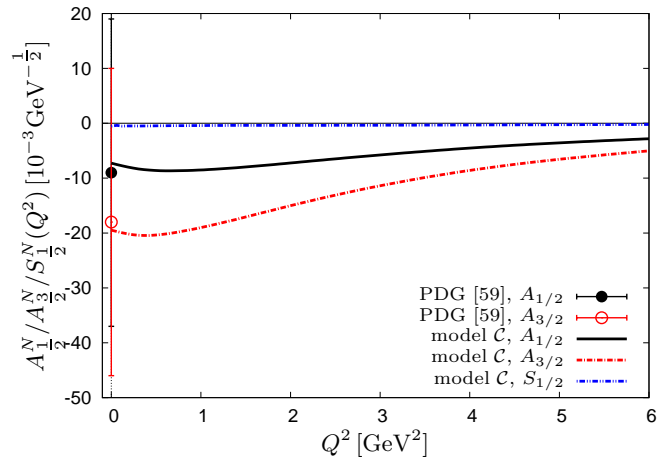


Fig. 52. Comparison of the $D_{35}(1930)$ helicity amplitudes $A_{1/2}^N$ (black line), $A_{3/2}^N$ (red line) and $S_{1/2}^N$ (blue line) calculated in model \mathcal{C} with the PDG-data [59]. See also caption to Fig. 6.

model \mathcal{C} are slightly smaller than those in model \mathcal{A} . In both cases the longitudinal amplitude virtually vanishes.

3.2 Photon couplings

In tables 2 and 3 we have summarised the results for the photon decay amplitudes as partially already discussed in subsections 3.1.1 and 3.1.2. This tables also lists the available experimental data. Most of the decay amplitudes can be accounted for quite satisfactory. In general no large differences between both models is found. For some amplitudes of resonances with higher angular momentum no experimental data are available to our knowledge.

Table 2. Transverse photon couplings calculated for $N \rightarrow N^*$ transitions in model \mathcal{A} and \mathcal{C} in comparison to experimental data. All calculated photon couplings were determined by calculating the helicity amplitudes at $Q^2 = 10^{-4} \text{ GeV}^2$ close to the photon point. A hyphen indicates that data do not exist. All amplitudes are in units of $10^{-3} \text{ GeV}^{-1/2}$, all masses are given in MeV. The references [76, 78] do not quote errors.

State	Rat.	Mass		Ampl.	Model \mathcal{A}		Model \mathcal{C}		Exp.		Ref.
		model \mathcal{A}	model \mathcal{C}		p	n	p	n	p	n	
$S_{11}(1535)$	****	1417	1475	$A_{1/2}$	111.68	-74.75	85.93	-54.96	90 ± 30	-46 ± 27	[59]
$S_{11}(1650)$	****	1618	1681	$A_{1/2}$	2.55	-16.03	-4.56	-6.86	53 ± 16	-15 ± 21	[59]
$S_{11}(1895)$	**	1872	1839	$A_{1/2}$	43.36	-23.93	52.71	-29.01	12 ± 6	-	[17]
		1886	1882		38.95	-18.44	17.18	-8.27			
$P_{11}(1440)$	****	1498	1430	$A_{1/2}$	33.51	-18.68	33.10	-17.43	-60 ± 4	40 ± 10	[59]
$P_{11}(1710)$	***	1700	1712	$A_{1/2}$	58.36	-30.59	30.95	-13.57	24 ± 10	-2 ± 14	[59]
$P_{11}(1880)$	**	1905	1872	$A_{1/2}$	24.35	-15.55	24.44	-11.87	14 ± 3	-	[17]
$P_{13}(1720)$	****	1655	1690	$A_{1/2}$	81.69	-33.06	50.28	-22.56	18 ± 30	1 ± 15	[59]
				$A_{3/2}$	-26.24	11.76	-17.10	2.69	-19 ± 20	-29 ± 61	[59]
$P_{13}(1900)$	***	1859 1894	1840	$A_{1/2}$	5.06	3.17	2.31	5.17	$26 \pm 15 / -17$	$- / -16$	[17] / [76]
					12.58	-14.53					
				$A_{3/2}$	2.29	18.15	4.03	13.79	$-65 \pm 30 / 31$	$- / -2$	[17] / [76]
					6.49	-14.90					
$D_{13}(1520)$	****	1453	1520	$A_{1/2}$	-54.80	2.47	-39.39	0.65	-24 ± 9	-59 ± 9	[59]
$D_{13}(1700)$	***	1573	1686	$A_{3/2}$	48.45	-52.27	32.80	-31.64	150 ± 15	-139 ± 11	[59]
				$A_{1/2}$	-20.69	16.52	-10.16	10.65	-18 ± 13	0 ± 50	[59]
$D_{13}(1875)$	***	1896 1920	1849 1921	$A_{3/2}$	-5.45	38.89	-7.08	26.42	-2 ± 24	-3 ± 44	[59]
				$A_{1/2}$	49.87	-19.04	42.29	-13.71	$18 \pm 10 / -20 \pm 8$	7 ± 13	[17] / [74] / [59] / [76] / [79]
				$A_{3/2}$	1.62	-6.73	-3.72	-6.76	$12 / 26 \pm 52$		[17] / [74] / [59] / [76] / [79]
					-20.86	13.11	-21.46	10.17	$-9 \pm 5 / 17 \pm 11$	-53 ± 34	[17] / [74] / [59] / [76] / [79]
					-5.78	-2.38	0.64	-4.27	$-10 / 128 \pm 57$		
$D_{15}(1675)$	****	1623	1678	$A_{1/2}$	3.74	-25.80	6.16	-19.91	19 ± 8	-43 ± 12	[59]
$D_{15}(2060)$	**	1935 2063	1922 2017	$A_{3/2}$	5.39	-36.41	-1.36	-22.98	15 ± 9	-58 ± 13	[59]
				$A_{1/2}$	50.63	-28.09	26.71	-16.48	65 ± 12	-	[17]
				$A_{3/2}$	0.83	-14.53	2.74	-12.84			
					-17.97	10.01	-8.99	2.06	55^{+15}_{-35}	-	[17]
					1.35	-20.16	-2.92	-17.67			
$F_{15}(1680)$	****	1695	1734	$A_{1/2}$	-45.91	32.65	-29.98	22.25	-15 ± 6	29 ± 10	[59]
				$A_{3/2}$	42.16	-12.85	24.10	-6.95	133 ± 12	-33 ± 9	[59]
$F_{15}(1860)$	**	1892 1918	1933 1978	$A_{1/2}$	-9.86	-11.41	1.22	-13.86	20 ± 12	-	[17]
				$A_{3/2}$	-5.33	17.12	-5.41	4.31			
$F_{15}(2000)$	**	2082	1978 2062	$A_{3/2}$	-0.41	-23.28	-0.60	-11.28	50 ± 20	-	[17]
				$A_{1/2}$	-5.34	6.48	-2.21	-2.67			
				$A_{3/2}$	-0.05	0.59	-5.41	4.31	35 ± 15	-	[17]
								32.96	-21.35		
					-0.02	0.61	-2.21	-2.70	50 ± 14	-	[17]
							-16.72	6.06			
$F_{17}(1990)$	**	1954	1997	$A_{1/2}$	-2.98	-9.19	-3.94	-3.22	$42 \pm 14 / 30 \pm 29$	$- / -1$	[17] / [74]
				$A_{3/2}$	-3.96	-11.81	0.39	-5.88	40	-69	[78]
									$58 \pm 12 / 86 \pm 60$	$- / -178$	[17] / [74]
									4	-72	[78]
$G_{17}(2190)$	****	1986	1980	$A_{1/2}$	-27.72	8.47	-12.42	2.69	-65 ± 8	-	[17]
				$A_{3/2}$	19.04	-13.45	8.80	-6.48	35 ± 17	-	[17]
$G_{19}(2250)$	****	2181	2169	$A_{1/2}$	1.26	-11.16	2.18	-6.65	$ A_{1/2}^p < 10$	-	[17]
				$A_{3/2}$	1.64	-13.70	-0.27	-6.54	$ A_{1/2}^p < 10$	-	[17]
$H_{19}(2220)$	****	2183	2159	$A_{1/2}$	22.06	-13.65	10.63	-6.93	$ A_{1/2}^p < 10$	-	[17]
				$A_{3/2}$	-17.40	7.04	-7.78	3.05	$ A_{1/2}^p < 10$	-	[17]
$I_{1,11}(2600)$	***	2394	2342	$A_{1/2}$	14.06	-5.45	-5.56	-1.89	-	-	-
				$A_{3/2}$	-10.07	5.97	-4.07	2.46	-	-	-

Table 3. Transverse photon couplings calculated for $N \rightarrow \Delta$ transitions in model \mathcal{A} and \mathcal{C} in comparison to experimental data. All calculated photon couplings were determined by calculating the helicity amplitudes at $Q^2 = 10^{-4} \text{ GeV}^2$ close to the photon point. A hyphen indicates that data do not exist. All amplitudes are in units of $10^{-3} \text{ GeV}^{-1/2}$, all masses are given in MeV. Reference [76] does not quote errors.

State	Rat.	Mass		Ampl.	Model \mathcal{A}	Model \mathcal{C}	Exp.	Ref.
		model \mathcal{A}	model \mathcal{C}					
$S_{31}(1620)$	****	1620	1636	$A_{1/2}$	16.63	15.33	27 ± 11	[59]
$S_{31}(1900)$	**	–	1956	$A_{1/2}$	–	-1.43	$59 \pm 16 / 29 \pm 8 / -4 \pm 16$	[17]/ [74]/ [75]
$P_{31}(1750)$	*	–	1765	$A_{1/2}$	–	6.27	53	[76]
$P_{31}(1910)$	****	1829/1869	1892	$A_{1/2}$	2.38/0.69	1.98	3 ± 14	[59]
$P_{33}(1232)$	****	1233	1231	$A_{1/2}$	-93.23	-68.08	-135 ± 6	[59]
$P_{33}(1600)$	***	–	1596	$A_{3/2}$	-158.61	-122.08	-250 ± 8	[59]
				$A_{1/2}$	–	-14.98	-23 ± 20	[59]
$P_{33}(1920)$	***	1834/1912	1899/1932	$A_{3/2}$	–	-35.24	-9 ± 21	[59]
				$A_{1/2}$	20.89/1.79	14.89/11.90	$130^{+30}_{-60} / 40 \pm 14 / 22 \pm 8 / -7$	[17]/ [74]/ [77]/ [76]
$D_{33}(1700)$	****	1594	1600	$A_{1/2}$	64.99	63.39	104 ± 15	[59]
				$A_{3/2}$	67.25	71.47	85 ± 22	[59]
$D_{33}(1940)$	**	–	1895/1959	$A_{1/2}$	–	-16.86/-14.98	$-36 \pm 58 / 160 \pm 40$	[74]/ [77]
				$A_{3/2}$	–	-12.56/-27.19	$-31 \pm 12 / 110 \pm 30$	[74]/ [77]
$D_{35}(1930)$	***	–	2022	$A_{1/2}$	–	-7.27	-9 ± 28	[59]
				$A_{3/2}$	–	-19.49	-18 ± 28	[59]
$F_{35}(1905)$	****	1860	1896	$A_{1/2}$	18.46	12.42	26 ± 11	[59]
				$A_{3/2}$	41.22	23.54	-45 ± 20	[59]
$F_{37}(1950)$	****	1918	1934	$A_{1/2}$	-24.80	-14.22	-76 ± 12	[59]
				$A_{3/2}$	-31.94	-18.62	-97 ± 10	[59]
$H_{39}(2420)$	****	2399	2363	$A_{1/2}$	11.62	4.92	–	–
				$A_{3/2}$	13.78	5.90	–	–

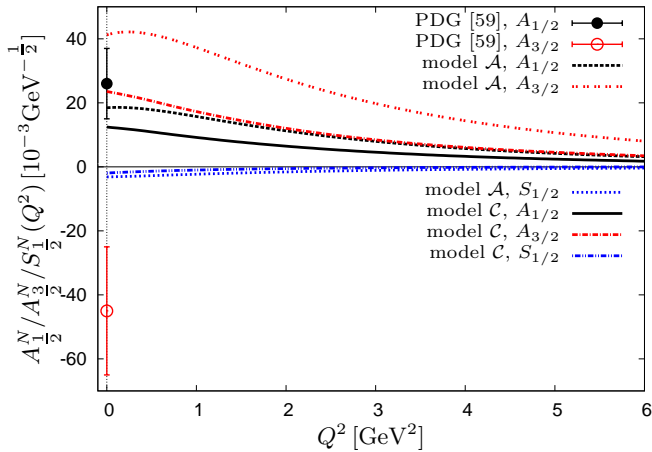


Fig. 53. Comparison of the $F_{35}(1905)$ transverse and longitudinal helicity amplitudes $A_{1/2}^N$, $A_{3/2}^N$ and $S_{1/2}^N$ calculated in model \mathcal{C} (solid and dashed-dotted line) and model \mathcal{A} (dashed lines). See also caption to Fig. 6.

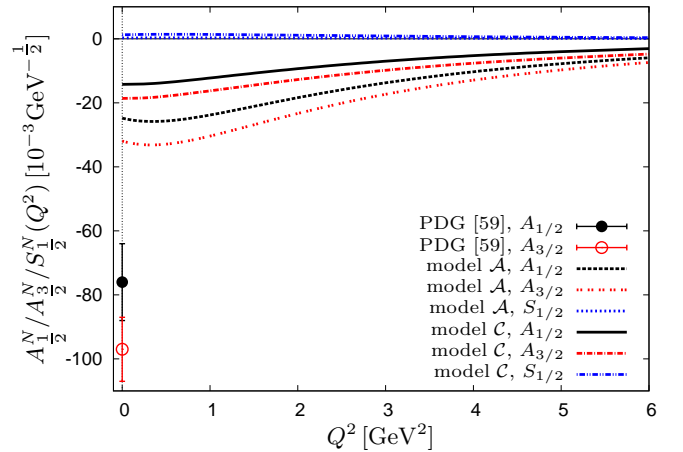


Fig. 54. Comparison of the $F_{37}(1950)$ transverse and longitudinal helicity amplitudes $A_{1/2}^N$, $A_{3/2}^N$ and $S_{1/2}^N$ calculated in model \mathcal{C} (solid and dashed-dotted line) and model \mathcal{A} (dashed lines). See also caption to Fig. 6.

3.3 The nucleon $\rightarrow \Delta(1232)$ transition form factors

The $N \rightarrow \Delta$ electric and magnetic transition form factors between the ground-state nucleon and the $P_{33}(1232)$ state

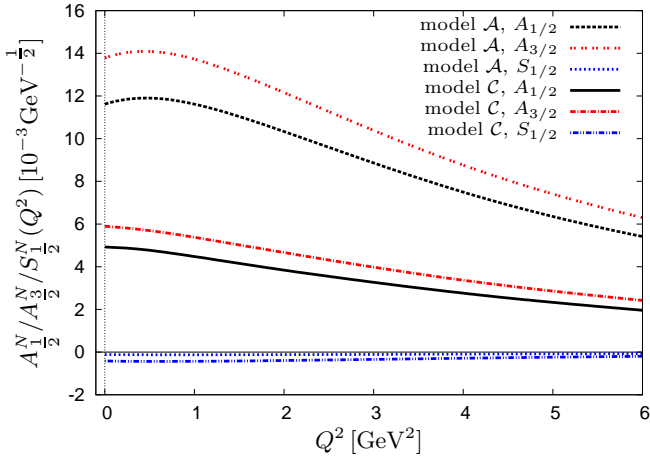


Fig. 55. Prediction of the $H_{311}(2420)$ transverse and longitudinal helicity amplitudes $A_{1/2}^N$, $A_{3/2}^N$ and $S_{1/2}^N$ calculated in model \mathcal{C} (solid and dashed-dotted line) and model \mathcal{A} (dashed lines). See also caption to Fig. 6.

are related to the helicity amplitudes by Eqs. (8a) and (8b)

$$G_E^*(Q^2) := F(Q^2) \left(\frac{1}{\sqrt{3}} A_{3/2}^N - A_{1/2}^N \right), \quad (8a)$$

$$G_M^*(Q^2) := F(Q^2) \left(\sqrt{3} A_{3/2}^N + A_{1/2}^N \right), \quad (8b)$$

respectively, where $F(Q^2)$ is a kinematical pre-factor defined as

$$F(Q^2) = -\sqrt{\frac{M_N}{4\pi\alpha} \frac{M_\Delta^2 - M_N^2}{2M_\Delta^2} \frac{M_N}{|\mathbf{k}|}} \quad (9)$$

in the notation of Ash *et al.* [80]. Furthermore, for the sake of completeness the Coulomb-transition form factor is given by

$$G_C^*(Q^2) = -2 \frac{M_\Delta}{|\mathbf{k}|} F(Q^2) \sqrt{2} S_{1/2}^N. \quad (10)$$

In Fig. 56 the calculated magnetic transition form factor divided by thrice the standard dipole form factor is compared to experimental data and analyses. This representation enhances the discrepancies between the calculated and experimental results: Although model \mathcal{A} still gives a fair description at larger momentum transfers, albeit in general too small, model \mathcal{C} yields too large values in this regime. In both models the values at low momenta are too small, a discrepancy which this calculation shares with virtually all calculations within a constituent quark model. Usually this is regarded to be an indication of effects due to the coupling to pions. In Fig. 57 we also present to corresponding electric transition form factor. Only model \mathcal{C} agrees with the PDG-data [59] of the MAID-analysis [22, 23], whereas model \mathcal{A} even has the wrong sign. In model \mathcal{A} we recalculated the form factor with a higher numerical accuracy than was done by Merten *et al.* in [5]. The Coulomb transition form factor is displayed in Fig. 58. Although the calculated result in model \mathcal{C} is significantly larger than in model \mathcal{A} , both are too small to account for the data from the MAID-analysis [22–24].

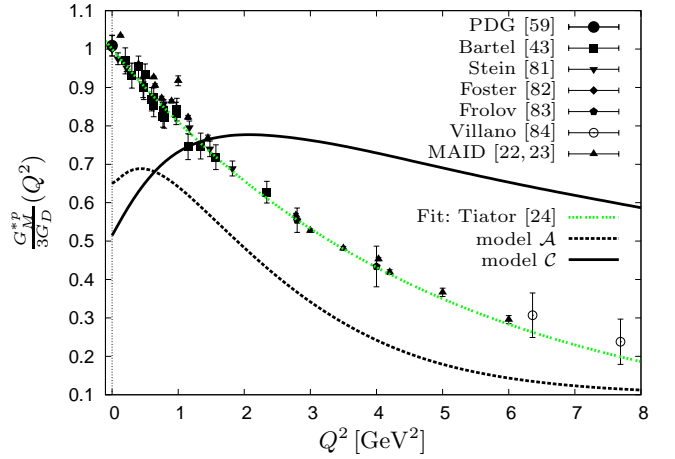


Fig. 56. Comparison of $\Delta(1232)$ magnetic transition form factor G_M^{*p} calculated within model \mathcal{C} (solid line) and model \mathcal{A} (dashed line). See also caption to Fig. 6.

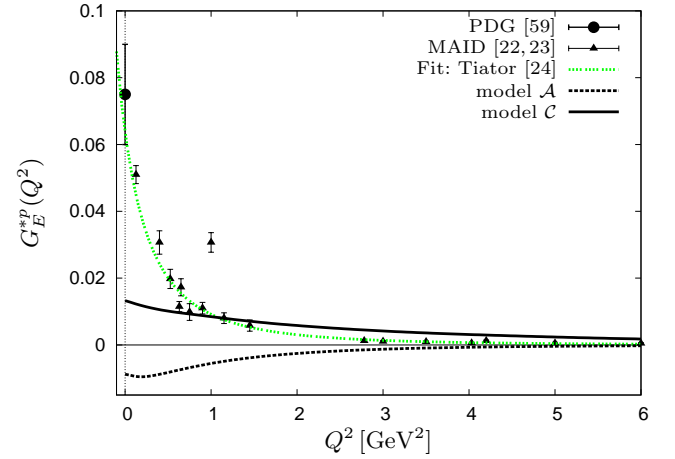


Fig. 57. Comparison of $\Delta(1232)$ electric transition form factor G_E^{*p} calculated within model \mathcal{C} (solid line) and model \mathcal{A} (dashed line). See also caption to Fig. 6.

4 Summary and conclusion

In this paper we supplement the investigation of a novel spin-flavour dependent interaction within the framework of a relativistically covariant constituent quark model for the structure of baryon resonances, as presented in [1] by a calculation of helicity amplitudes for electro-excitation of the nucleon. The calculational framework for the computation of current-matrix elements is the same as presented by Merten *et al.* [5]. In the current contribution the Salpeter-amplitudes were obtained in a calculation of the baryon mass spectra, see [1], where, in addition to confinement and a spin-flavour dependent interaction motivated by instanton effects as used in an older version called model \mathcal{A} , a phenomenological short ranged spin-flavour dependent interaction was introduced in order to improve in particular upon the description of some excited negative parity Δ resonances at ≈ 1.9 GeV; this novel version of the model is called \mathcal{C} . On the basis of these ampli-

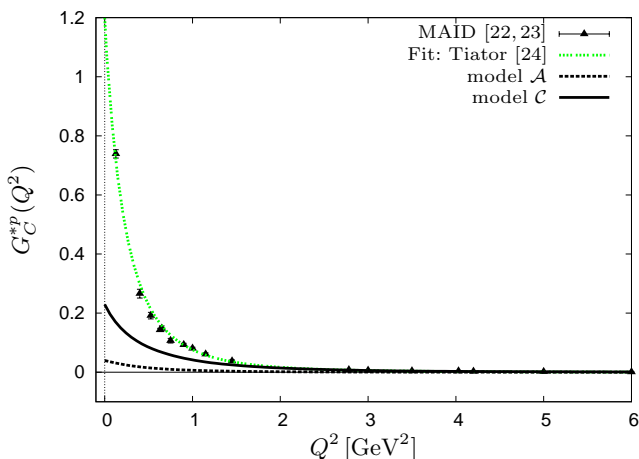


Fig. 58. Comparison of $\Delta(1232)$ Coulomb transition form factor G_C^{*p} calculated within model \mathcal{C} (solid line) and model \mathcal{A} (dashed line). See also caption to Fig. 6.

tudes the current-matrix elements relevant for the helicity amplitudes were calculated in lowest order without introducing any additional parameters. In the course of the investigations within the novel version of the relativistic quark model \mathcal{C} an improved parameter set was found as discussed in sec. 2. The modification affects mainly the neutron form factor which now rather accurately reproduces the experimental data.

The calculated results are compared to experimental data as far as available for resonances with a three or four star rating according to the PDG [59]. The experimental data comprise the couplings at the photon point from PDG [59] and [17] as well as recent determinations of transverse and longitudinal amplitudes as reported by Aznauryan [18–21] and in the MAID-analysis [22, 23], see also [24]. The results for the helicity amplitudes of nucleon resonances can be summarised as follows:

- A satisfactory description of data for the $S_{11}(1535)$, $P_{11}(1440)$, $D_{13}(1520)$ and $F_{15}(1680)$ data was found. Exceptions are: A node in the transverse $P_{11}(1440)$ -amplitude as found experimentally was not reproduced by the calculations; we also do not find the observed minimum in the longitudinal $S_{11}(1535)$ -amplitude and the calculations underestimate the transverse $S_{11}(1650)$ as well as the longitudinal $F_{15}(1680)$ -amplitude for low momentum transfers. Also the amplitudes of the $D_{13}(1520)$ resonances are slightly too small in model \mathcal{C} . Furthermore predictions of helicity amplitudes are given for higher excited resonances for both models. Some of these were recently found by [15–17], e.g. the $N_{1/2}^+(1880)$ and $N_{1/2}^-(1895)$ resonance.

For the nucleon- Δ transitions helicity amplitudes, as discussed in sec. 3.1.2, we note that:

- There exists agreement with the scarce data for the $S_{31}(1620)$ amplitude if we disregard two data points for the longitudinal amplitude. There is an indication for a sign disagreement between the data of Aznauryan *et al.* [19] and that for the MAID-analysis [22, 23] or

alternatively a node in the amplitude exists which is not reproduced by both models in this case.

- The $P_{33}(1232)$ helicity amplitudes are generally underestimated by both models, slightly more so in model \mathcal{C} . For the longitudinal amplitude in particular we find a maximum in the theoretical curves for which there exists no experimental evidence.
- Predictions of the negative parity excited $\Delta^*(1900, 1940, 1930)$ helicity amplitudes can be made in model \mathcal{C} . The position of these states cannot be reproduced in the original model \mathcal{A} and was the main motivation to supplement the dynamics of the model by an additional short-ranged spin-flavour dependent interaction. It is rewarding that the calculated photon decay amplitudes agree reasonably well with the PDG data for these three resonances.

In addition we presented predictions for helicity amplitudes of some lower rated resonances, such as $P_{31}(1750)$ and $D_{33}(1940)$ as well as predictions to some photon decay amplitudes analysed by the CB-ELSA collaboration *et al.* [17]. The corresponding photon decay amplitude data from the CB-ELSA collaboration are presently mostly included in the new PDG-data and thus only occasionally listed explicitly in table 2 and 3. For nucleon photon decay amplitudes displayed in table 2 we found that model \mathcal{C} reproduces the data of $A_{1/2}^p$ slightly better than model \mathcal{A} . The $A_{3/2}^p$ decay amplitudes in both models are too small in general. Analysing table 3 for Δ -transition amplitudes we find a slightly better agreement for model \mathcal{A} than for model \mathcal{C} .

For the magnetic form factor of the $\Delta(1232)$ - N transition we have found that both models cannot accurately account for the data, the calculated values being too small in model \mathcal{A} generally and in model \mathcal{C} for $Q^2 < 1.5 \text{ GeV}^2$. With the MAID-data [22,23] and the fits reported in [24] it becomes also possible to make a statement on the electric transition form factor which is better reproduced by model \mathcal{C} . Model \mathcal{A} even produces a wrong sign compared to the MAID-data. The momentum dependence of the Coulomb transition form factor is well described by model \mathcal{C} , but too small in magnitude by more than a factor 3. Model \mathcal{A} yields almost vanishing values in this case. The corresponding elastic nucleon form factors calculations were already presented in [1].

Although the overall agreement of calculated and experimental helicity data in both versions \mathcal{A} and \mathcal{C} of the relativistic quark models are of similar quality, the new model \mathcal{C} apart from accounting better for the baryon mass spectrum also does improve on specific observables such as the ground state form factors.

Acknowledgements

We gratefully acknowledge the assistance of Simon Tölle in optimising the program-code. We are indebted to the referee for a multitude of valuable comments and suggestions.

References

1. M. Ronniger, B.C. Metsch, Eur. Phys. J. A **47**, 162 (2011).
2. U. Löring, K. Kretzschmar, B.C. Metsch, H.R. Petry, Eur. Phys. J. A **10**, 309-346 (2001).
3. U. Löring, B.C. Metsch, H.R. Petry, Eur. Phys. J. A **10**, 395-446 (2001).
4. U. Löring, B.C. Metsch, H.R. Petry, Eur. Phys. J. A **10**, 447-486 (2001).
5. D. Merten, U. Löring, K. Kretzschmar, B.C. Metsch, H.R. Petry, Eur. Phys. J. A **14**, 477 (2002).
6. L. Ya. Glozman, D. O. Riska, Phys. Rep. **268**, 263-303 (1996).
7. L. Ya. Glozman, Z. Papp, W. Plessas, K. Varga and R. F. Wagenbrunn, Nucl. Phys. A **623**, 90-99 (1997).
8. L. Ya. Glozman, Z. Papp, W. Plessas, K. Varga and R. F. Wagenbrunn, Phys. Rev. C **57**, 3406 (1998).
9. L. Ya. Glozman, W. Plessas, K. Varga and R. F. Wagenbrunn, Phys. Rev. D **58**, 094030 (1998).
10. L. Theußl, R. F. Wagenbrunn, B. Desplanques and W. Plessas, Eur. Phys. J. A **12**, 91 (2001).
11. K. Glantschnig, R. Kainhofer, W. Plessas, B. Sengl and R. F. Wagenbrunn, Eur. Phys. J. A **23**, 507-515 (2005).
12. T. Melde, K. Berger, L. Canton, W. Plessas and R. F. Wagenbrunn Phys. Rev. D **76**, 074020 (2007).
13. T. Melde, W. Plessas, and B. Sengl, Phys. Rev. D **77**, 114002 (2008).
14. W. Plessas and T. Melde, AIP Conf. Proc. **1056**, 15-22 (2008).
15. A.V. Anisovich, E. Klempt, V.A. Nikonov, A.V. Sarantsev and U. Thoma, Eur. Phys. J. A **47**, 27 (2011).
16. A.V. Anisovich, V.A. Nikonov, A.V. Sarantsev, U. Thoma and E. Klempt, Eur. Phys. J. A **47**, 153 (2011).
17. A.V. Anisovich, R. Beck, E. Klempt, V.A. Nikonov, A.V. Sarantsev and U. Thoma, Eur. Phys. J. A **48**, 15 (2012).
18. I. G. Aznauryan, V. D. Burkert, H. Egiyan, K. Joo, R. Minehart, and L. C. Smith, Phys. Rev. C **71**, 015201 (2005).
19. I. G. Aznauryan, V. D. Burkert, G. V. Fedotov, B. S. Ishkhanov, and V. I. Mokeev, Phys. Rev. C **72**, 045201 (2005).
20. I. G. Aznauryan, V. D. Burkert, Phys. Rev. C **80**, 055203 (2009).
21. I. G. Aznauryan, V. D. Burkert, Prog. Part. Nucl. Phys. **67**, 1 (2012).
22. D. Drechsel, S. S. Kamalov, and L. Tiator, Eur. Phys. J. A **34**, 69 (2007).
23. L. Tiator, D. Drechsel, S. S. Kamalov, M. Vanderhaeghen, Chinese Phys. C **33**, 1069 (2009).
24. L. Tiator, D. Drechsel, S. S. Kamalov and M. Vanderhaeghen, Eur. Phys. J. Special Topics **198**, 141 (2011).
25. S. Kreuzer, *Ein masseabhängiges Confinement-Potential für das Bethe-Salpeter-Modell*, Diploma thesis, University of Bonn, (2006).
26. D. Merten, *'Hadron Form factors and Decays'* PhD thesis, University of Bonn (2002).
27. P. Mergell, U.-G. Meißner and D. Drechsel, Nucl. Phys. A **596**, 367 (1996).
28. A. Bodek, S. Avvakumov, R. Bradford, and H. Budd, J. Phys. Conf. Ser. **110**, 082004 (2008).
29. M.E. Christy *et al.*, Phys. Rev. C **70**, 015206 (2004).
30. I. A. Qattan *et al.*, Phys. Rev. Lett. **94**, 142301 (2005).
31. T. Eden *et al.*, Phys. Rev. C **50**, 1749 (1994).
32. C. Herberg *et al.*, Eur. Phys. J. A **5**, 131 (1999).
33. M. Ostrick *et al.*, Phys. Rev. Lett. **83**, 276 (1999).
34. I. Passchier *et al.*, Phys. Rev. Lett. **82**, 4988 (1999).
35. R. Schiavilla *et al.*, Phys. Rev. C **64**, 041002 (2001).
36. D. Rohe *et al.*, Phys. Rev. Lett. **83**, 21 (1999).
37. J. Golak *et al.*, Phys. Rev. C **63**, 034006 (2001).
38. H. Zhu *et al.*, Phys. Rev. Lett. **87**, 081801 (2001).
39. R. Madey *et al.*, Phys. Rev. Lett. **91**, 122002 (2003).
40. G. Warren *et al.*, Phys. Rev. Lett. **92**, 042301 (2004).
41. D. I. Glazier *et al.*, Eur. Phys. J. A **24**, 101 (2005).
42. R. Alarcon *et al.*, Eur. Phys. J. A **31**, 588 (2007).
43. T. Bartel *et al.*, Nucl. Phys. B **58**, 469 (1973).
44. H. Anklin *et al.*, Phys. Lett. B **428**, 248 (1998).
45. W. Xu *et al.*, Phys. Rev. Lett. **85** (2000).
46. G. Kubon *et al.*, Phys. Lett. B **524**, 26 (2002).
47. E. Amaldi *et al.*, Phys. Lett. B **41**, 216 (1972).
48. P. Brauel *et al.*, Phys. Lett. B **45**, 389 (1973).
49. E. D. Bloom *et al.*, Phys. Rev. Lett. **30**, 1186 (1973).
50. A. Del Guerra *et al.*, Nucl. Phys. B **99**, 253 (1975).
51. P. Joos *et al.*, Phys. Lett. B **62**, 230 (1976).
52. N. J. Baker *et al.*, Phys. Rev. D **23**, 2499 (1981).
53. K. L. Miller *et al.*, Phys. Rev. D **26**, 537 (1982).
54. T. Kitagaki *et al.*, Phys. Rev. D **28**, 436 (1983).
55. T. Kitagaki *et al.*, Phys. Rev. D **42**, 1331 (1990).
56. D. Allasia *et al.*, Nucl. Phys. B **343**, 285 (1990).
57. V. Bernard, L. Elouadrhiri, and U.-G. Meißner, J. Phys. G **28**, 1-35 (2002).
58. M. Warns *et al.*, Z. Phys. C **45**, 627 (1990).
59. J. Beringer *et al.* (Particle Data Group), Phys. Rev. D **86**, 010001 (2012)
60. P. Kummer *et al.*, Phys. Rev. Lett. **30**, 873 (1973).
61. U. Beck *et al.*, Phys. Lett. B **51**, 103 (1974).
62. J. Alder *et al.*, Nucl. Phys. B **91**, 386 (1975).
63. H. Breuer *et al.*, Phys. Lett. B **74**, 409 (1978).
64. F. W. Brasse *et al.*, Nucl. Phys. B **139**, 37 (1978).
65. M. Benmerrouche *et al.*, Phys. Rev. Lett. **67**, 1070 (1991).
66. B. Krusche *et al.*, Phys. Rev. Lett. **74**, 3736 (1995).
67. C. S. Armstrong *et al.*, Phys. Rev. D **60**, 052004 (1999).
68. R. Thompson *et al.*, Phys. Rev. Lett. **86**, 1702 (2001).
69. B. D. Keister and S. Capstick, N* PHYSICS, edited by T.-S. H. Lee and W. Roberts, 341 World Scientific, Singapore (1997).
70. S. Capstick and B. D. Keister, Phys. Rev. D **51**, 3598 (1995).
71. V. Burkert, *Reserach Program at CEBAF II*, edited by V. Burkert *et al.*, CEBAF (USA), 161 (1986).
72. C. Gerhardt, Z. Phys. C **4**, 311 (1980).
73. J. Ahrens *et al.*, Phys. Rev. Lett. **88**, 232002 (2002).
74. N. Awaji *et al.*, DPNU-29-81, (1981) 11.
75. C. B. Crawford *et al.*, Phys. Rev. Lett. **98**, 052301 (2007).
76. G. Penner, U. Mosel, Phys. Rev. C **66**, 055212 (2002).
77. I. Horn *et al.*, Eur. Phys. J. A **38**, 173 (2008).
78. I. M. Barbour, R. L. Crawford and N. H. Parsons, Nucl. Phys. B **141**, 253 (1978).
79. R. C. E. Devenish D. H. Lyth and W. A. Rankin, Phys. Lett. B **52**, 227 (1974).
80. W. W. Ash, K. Berkelman, C. A. Lichtenstein, A. Ramanaukas and R. H. Siemann Phys. Lett. B **24**, 165 (1967).
81. S. Stein *et al.*, Phys. Rev. D **12**, 1884 (1975).
82. F. Foster and G. Hughes, Rep. Prog. Phys. **46**, 1445 (1983).
83. V. V. Frolov *et al.*, Phys. Rev. Lett. **82**, 45 (1999).
84. A. N. Villano *et al.*, Phys. Rev. C **80**, 035203 (2009).